

**Key Points:**

- We present the most complete time-resolved paleointensity record for five Main Group (MG) pallasites
- Paleointensities require the MG pallasites to have formed in a thin mantle overlying a large metallic core
- The MG pallasites could have originated from a parent body with a similar structure to the asteroid (16) Psyche

**Supporting Information:**

Supporting Information may be found in the online version of this article.

**Correspondence to:**

C. I. O. Nichols,  
[claire.nichols@earth.ox.ac.uk](mailto:claire.nichols@earth.ox.ac.uk)

**Citation:**

Nichols, C. I. O., Bryson, J. F. J., Cottrell, R. D., Fu, R. R., Harrison, R. J., Herrero-Albillos, J., et al. (2021). A time-resolved paleomagnetic record of Main Group pallasites: Evidence for a large-cored, thin-mantled parent body. *Journal of Geophysical Research: Planets*, 126, e2021JE006900. <https://doi.org/10.1029/2021JE006900>

Received 8 APR 2021

Accepted 15 JUN 2021

**Author Contributions:**

**Data curation:** Claire I. O. Nichols, James F. J. Bryson, Rory D. Cottrell, Roger R. Fu, Julia Herrero-Albillos, Florian Kronast

**Formal analysis:** Claire I. O. Nichols

**Funding acquisition:** Claire I. O. Nichols, Richard J. Harrison, John A. Tarduno, Benjamin P. Weiss

**Investigation:** Claire I. O. Nichols, Rory D. Cottrell, Julia Herrero-Albillos, Florian Kronast

**Project Administration:** Richard J. Harrison

© 2021. The Authors.

This is an open access article under the terms of the [Creative Commons Attribution License](https://creativecommons.org/licenses/by/4.0/), which permits use, distribution and reproduction in any medium, provided the original work is properly cited.

## A Time-Resolved Paleomagnetic Record of Main Group Pallasites: Evidence for a Large-Cored, Thin-Mantled Parent Body

Claire I. O. Nichols<sup>1,2</sup> , James F. J. Bryson<sup>2</sup>, Rory D. Cottrell<sup>3</sup> , Roger R. Fu<sup>4</sup> , Richard J. Harrison<sup>5</sup> , Julia Herrero-Albillos<sup>6,7</sup> , Florian Kronast<sup>8</sup>, John A. Tarduno<sup>3</sup> , and Benjamin P. Weiss<sup>1</sup> 

<sup>1</sup>Department of Earth, Atmospheric and Planetary Sciences, Massachusetts Institute of Technology, Cambridge, MA, USA, <sup>2</sup>Department of Earth Sciences, University of Oxford, Oxford, UK, <sup>3</sup>Department of Earth and Environmental Sciences, University of Rochester, Rochester, NY, USA, <sup>4</sup>Department of Earth and Planetary Sciences, Harvard University, Cambridge, MA, USA, <sup>5</sup>Department of Earth Sciences, University of Cambridge, Cambridge, UK, <sup>6</sup>Departamento de Ciencia y Tecnología de Materiales y Fluidos, Universidad de Zaragoza, Zaragoza, Spain, <sup>7</sup>Instituto de Nanociencia y Materiales de Aragón (INMA), CSIC—Universidad de Zaragoza, Zaragoza, Spain, <sup>8</sup>Helmholtz-Zentrum Berlin für Materialien und Energie, Berlin, Germany

**Abstract** Several paleomagnetic studies have been conducted on five Main Group pallasites: Brenham, Marjalahti, Springwater, Imilac, and Esquel. These pallasites have distinct cooling histories, meaning that their paleomagnetic records may have been acquired at different times during the thermal evolution of their parent body. Here, we compile new and existing data to present the most complete time-resolved paleomagnetic record for a planetesimal, which includes a period of quiescence prior to core solidification as well as dynamo activity generated by compositional convection during core solidification. We present new paleomagnetic data for the Springwater pallasite, which constrains the timing of core solidification. Our results suggest that in order to generate the observed strong paleointensities ( $\sim 65\text{--}95\ \mu\text{T}$ ), the pallasites must have been relatively close to the dynamo source. Our thermal and dynamo models predict that the Main Group pallasites originate from a planetesimal with a large core ( $>200\ \text{km}$ ) and a thin mantle ( $<70\ \text{km}$ ).

**Plain Language Summary** We have studied five pallasite meteorites which are composed of a green mineral called olivine surrounded by iron–nickel metal. These meteorites are all thought to originate from the same parent asteroid. We have measured the magnetism of these meteorites and recovered information about the magnetic fields they experienced when they initially formed and cooled. Our magnetic measurements show that the parent asteroid generated its own magnetic field, suggesting that the asteroid had a metallic core that was vigorously convecting. We find that our results are best explained by the parent asteroid having a large metal core and a thin rocky shell.

### 1. Introduction

The Main Group (MG) pallasites are all thought to originate from the same planetesimal (Greenwood et al., 2006). Temporal variations in core dynamo activity on this parent asteroid have been shown by several paleomagnetic studies. For instance, Tarduno et al. (2012) found the first evidence for dynamo activity recorded by magnetic inclusions in olivine crystals from the Imilac and Esquel pallasites. This observation was supported by a paleomagnetic study of the cloudy zone in the Imilac and Esquel pallasites (Bryson et al., 2015). Both studies retrieved paleointensities of  $\sim 100\ \mu\text{T}$ , interpreted as evidence for an active dynamo  $\sim 140\text{--}240\ \text{Myr}$  after parent body accretion. An active thermal dynamo is predicted to have only lasted for a maximum of  $\sim 40\ \text{Myr}$  after accretion (Bryson, Neufeld, et al., 2019; Dodds et al., 2021; Elkins-Tanton et al., 2011). Therefore, this measured magnetic remanence has instead been attributed to compositional convection resulting from core solidification. A subsequent paleomagnetic study of the cloudy zone in the Marjalahti and Brenham pallasites found no evidence of an active dynamo  $\sim 100\text{--}120\ \text{Myr}$  after accretion (Nichols et al., 2016). Dynamo initiation and the onset of core solidification was therefore predicted to occur between the time at which Brenham and Marjalahti, and subsequently Imilac and Esquel, acquired their paleomagnetic records.

**Supervision:** Richard J. Harrison, John A. Tarduno, Benjamin P. Weiss

**Writing – original draft:** Claire I. O. Nichols

**Writing – review & editing:** Claire I. O. Nichols, James F. J. Bryson, Rory D. Cottrell, Roger R. Fu, Richard J. Harrison, John A. Tarduno, Benjamin P. Weiss

Paleomagnetic signals are recorded by two mechanisms in pallasites. Magnetic inclusions of taenite (with 50–55 wt% Ni) within the olivine crystals acquire a thermal remanent magnetization (TRM) upon cooling below their blocking temperature between 360°C and 500°C (Tarduno et al., 2012). The cloudy zone (an FeNi microstructure that forms as part of the Widmanstätten pattern in meteoritic metal) acquires a chemical transformation remanent magnetization when tetraetaenite ordering occurs below 320°C (Einsle et al., 2018). Therefore, the timing of remanence acquisition for both of these mechanisms is dependent on cooling rate; slower-cooled pallasites will record paleomagnetic signals at a later time than fast-cooled pallasites.

Here, we investigate paleomagnetic signals recorded by the Springwater pallasite cloudy zone using X-ray photoemission electron microscopy (X-PEEM) and reassess the signals recorded by the cloudy zones of Brenham, Marjalahti, Imilac, and Esquel with the aim of better understanding this dynamo record and its implications for the thermal history and structure of the parent body. Springwater has an intermediate cooling rate among these five pallasites, so has the potential to capture the onset of core solidification and the initiation of a compositionally driven dynamo. We also assess the rock magnetic and paleomagnetic behavior of magnetic inclusions in olivines from the Imilac and Springwater pallasites in an attempt to reconcile paleointensity estimates from X-PEEM with those measured using more traditional paleomagnetic techniques (e.g., the Thellier–Thellier method).

Previous studies assumed the MG pallasite parent body had a radius of 200 km and a core with radius 100 km in order for the core to be at least partially molten when Imilac and Esquel acquired a record of the dynamo (Bryson et al., 2015; Nichols et al., 2016; Tarduno et al., 2012). These studies also assumed that the dynamo was generated by the outward solidification of an inner core (Nimmo, 2009) and that the core contained 31 wt% sulfur and therefore solidified at the FeS eutectic (Ehlers, 1972). Here, we consider a range of sulfur compositions and their effect on the timing of core solidification. Given the small size of the planetesimal, we also consider nucleation at the core–mantle boundary and inward core solidification (Williams, 2009), and the impact of this on dynamo generation.

The pallasites have an enigmatic formation history. They have commonly been interpreted to represent the core–mantle boundary, but this has been questioned given their paleomagnetic record of the dynamo, which suggests that they must have formed at a much lower temperature than the molten core (Bryson et al., 2015; Mckibbin et al., 2019; Nichols et al., 2016; Tarduno et al., 2012). In addition, their varied cooling rates have been used to argue that they formed at a variety of depths in a disorganized asteroid reassembled after impact (Yang et al., 2010). Most recently, it has been suggested that the pallasites could originate from a mantle-stripped metallic asteroid, such as asteroid (16) Psyche (Elkins-Tanton et al., 2020). This would resolve the discrepancy between shallow and deep origins for the pallasites, if they originate in the middle of thin mantle that is a short distance from the core–mantle boundary. To resolve the pallasite controversy, Tarduno et al. (2012) suggested an impact whereby dykes from the impactor core penetrated into the parent body mantle. Alternatively, Johnson et al. (2019) recently suggested a mechanism for pallasite formation by which sulfur-rich metallic melts at the core–mantle boundary penetrate a shallow overlying mafic mantle. These authors also suggest that the paleomagnetic record of the pallasites may be consistent with a dynamo driven by inward core solidification (Neufeld et al., 2019; Scheinberg et al., 2016).

Here, we present the most complete paleomagnetic record yet of the MG pallasite parent body. We report a new X-PEEM paleointensity for the Springwater pallasite cloudy zone and compile previous paleointensity measurements of the cloudy zone and olivine inclusions in the Brenham, Marjalahti, Imilac, and Esquel pallasites. We discuss the implications for the size, internal structure, and nature of core solidification on the parent body. We argue that the pallasites may originate from a parent body similar to the metallic asteroid (16) Psyche and could originate from within a thin mantle above, but closer to, the core–mantle boundary.

## 2. Samples and Methods

### 2.1. X-Ray Photoemission Electron Microscopy of the Cloudy Zone

#### 2.1.1. Sample Preparation

A sample of Springwater (BM 1959,1017) was borrowed from the Natural History Museum, London. A 5 × 5 mm section was cut using a tile saw and thinned using a lapping wheel in the presence of water

to prevent heating. The sample was then polished with diamond paste grade 9–0.25  $\mu\text{m}$ . The sample was etched for  $\sim 30$  s with nital (2% nitric acid in ethanol) to reveal the FeNi microstructures and was examined using reflected light microscopy to ensure there was no evidence of terrestrial weathering or shock. The sample was then repolished and sputtered for 10 h at 1.2 keV, 12 h at 0.8 keV, and 1.5 h at 0.4 keV using a focused Ar-ion beam under ultra-high vacuum (pressure  $< 1.5 \times 10^{-5}$  mbar) to remove any oxidation and surface magnetization induced by polishing and to minimize surface topography due to differential etching. The sample was kept in vacuum between sputtering and measuring (measuring pressure  $< 1.0 \times 10^{-8}$  mbar).

### 2.1.2. Experimental Method

X-PEEM measurements were performed at the SPEEM UE49 beamline, BESSY II, Berlin (Kronast et al., 2010). A beam of monochromatic X-rays was focused at  $16^\circ$  to the sample surface, exciting secondary photoelectrons from the top  $\sim 5$  nm of the sample surface. The X-rays were tuned to the Fe  $L_3$  edge ( $\sim 707$  eV) and linearly polarized to acquire compositional images. Images of the projection of the magnetic moment onto the X-ray beam were acquired using X-ray magnetic circular dichroism (XMCD). Images were acquired with a  $10 \mu\text{m}$  field of view (with a pixel size of  $19 \times 19$  nm). In total, 160 images were collected (80 for each polarization) with an exposure time of 2 s, and then averaged. Averaged images were also corrected for intensity drift due to minor sample charging (see Section S1.1.1).

The X-PEEM technique has been further developed since previous experiments, which only measured one magnetization component (Bryson et al., 2014, 2015; Nichols et al., 2016, 2018). We imaged Springwater using the three rotation approach outlined by Bryson et al. (2019), which enables the full vector magnetization to be recovered. Once the length of the tetrataenite rim-cloudy zone interface had been imaged, the sample was rotated  $109^\circ$  and the same interface was remeasured; the sample was then rotated  $120^\circ$  and remeasured, resulting in three data sets at different angles relative to the X-ray beam. We collected 12, 8, and 7 averaged and corrected images for rotations 1, 2, and 3, respectively.

### 2.1.3. Paleointensity Estimates

The magnitude and direction of the paleomagnetic field recorded by the Springwater cloudy zone was determined following the method outlined by Bryson et al. (2019). The mean XMCD intensities in each of the three measured orientations ( $I_1$ ,  $I_2$ , and  $I_3$ ) were used to reconstruct the 3D vector representing the paleomagnetic field at the time of remanence acquisition:

$$I_1 \approx \frac{M_s V}{6k_B T_0} ((I_{-x} - I_x)B_x + (I_{-y} - I_y)B_y + (I_{-z} - I_z)B_z) + \frac{1}{6}(I_x + I_{-x} + I_y + I_{-y} + I_z + I_{-z}) \quad (1)$$

$$I_2 \approx \frac{M_s V}{6k_B T_0} ((I'_{-x} - I'_x)B_x + (I'_{-y} - I'_y)B_y + (I'_{-z} - I'_z)B_z) + \frac{1}{6}(I'_x + I'_{-x} + I'_y + I'_{-y} + I'_z + I'_{-z}) \quad (2)$$

$$I_3 \approx \frac{M_s V}{6k_B T_0} ((I''_{-x} - I''_x)B_x + (I''_{-y} - I''_y)B_y + (I''_{-z} - I''_z)B_z) + \frac{1}{6}(I''_x + I''_{-x} + I''_y + I''_{-y} + I''_z + I''_{-z}) \quad (3)$$

where  $M_s$  is the saturation magnetization of tetrataenite ( $1.12 \times 10^6 \text{ Am}^{-1}$ ),  $V$  is the volume of tetrataenite islands at the time of remanence acquisition, which we take to be 78% of their present-day size (Maurel et al., 2019),  $k_B$  is the Boltzmann constant, and  $T_0$  is the tetrataenite formation temperature (593 K). The domains in the tetrataenite rim correspond to the XMCD intensities of the orthogonal easy axes  $I_x$ ,  $I_{-x}$ ,  $I_y$ ,  $I_{-y}$ ,  $I_z$ , and  $I_{-z}$  (Table S3). Although the tetrataenite rim intensities do not directly correspond to one another in different rotations (i.e., we did not measure the exact same field of view for each rotation), the uncertainty in how the intensities change with rotation has a negligible effect ( $< 1 \mu\text{T}$ ) on the calculated paleointensity.

Previously calculated paleointensities for the pallasites (Bryson et al., 2015; Nichols et al., 2016) are also reassessed here. Since these estimates were based on one measurement orientation, they represent lower

**Table 1**  
Summary of the Samples, Preparation Techniques, and Experimental Methods Used in This Study

Sample name	Pallasite	Loaned from	Sample preparation	Experimental methods
BM 1959,1017	Springwater	Natural History Museum, London	Polishing, etching, and sputtering of metal	X-PEEM
SWH	Springwater	Harvard Museum of Natural History	Diamond wire saw used to isolate oriented olivine cubes	AF demagnetization, IZZI Thellier (controlled-atmosphere furnace), SEM
SWR	Springwater	Harvard Museum of Natural History	Copper hammer/chisel used to “pop” entire olivines, then soaked in HCl acid	IZZI Thellier (CO <sub>2</sub> laser heating)
SW	Springwater	American Museum of Natural History	Diamond wire saw used to isolate oriented olivine cubes	AF demagnetization
IM	Imilac	Meteorite Madness	Diamond wire saw used to isolate oriented olivine cubes	AF demagnetization, IZZI Thellier (controlled-atmosphere furnace), SEM, QDM

*Note.* The first column lists the sample name used in this manuscript, the second column lists the pallasite studied, the third column lists the origin of the sample, the fourth column lists how the sample was prepared, and the fifth column lists the experimental methods used.

limits on the paleointensity, since it is unknown how the paleofield vector relates to the measurement direction. If the paleomagnetic field direction is parallel to the measurement direction, 100% of the paleointensity is recovered, whereas if the field is perpendicular to the measurement direction, 0% of the paleointensity is recovered. The recovered paleointensity ( $I_{rec}$ ) is proportional to the true paleointensity of the natural remanent magnetization ( $I_{NRM}$ ) depending on the angle,  $\theta$ , between the measurement direction and the paleofield vector:

$$I_{rec} = I_{NRM} \sin \theta \quad (4)$$

We calculated the 95% confidence for  $I_{NRM}$  by bootstrapping over all possible values of  $\theta$ . We sampled 100,000 values of  $\theta$  distributed evenly over a sphere for the measured values of  $I_{rec}$  for Brenham, Marjalahti, Imilac, and Esquel. We recovered a one-tailed distribution of values for  $I_{NRM}$  for each sample. Details of the bootstrapping method are given in the supplementary material, section S1.1.2.

## 2.2. Paleomagnetism and Rock Magnetism of Olivine Inclusions

### 2.2.1. Sample Preparation

Samples of Springwater were borrowed from the American Museum of Natural History (SW) and the Bowers Q.D. Collection, Harvard Museum of Natural History. A sample of Imilac (IM) was purchased from the meteorite collector “Meteorite Madness.” A summary of the samples used in this study and the associated preparation and experimental techniques is shown in Table 1. Samples were selected following the same protocol as Tarduno et al. (2012); regions of gem-quality olivines showing no visible inclusions were preferentially sampled. Gem-quality olivines are identified by conchoidal fracture, green coloration (rather than orange, which suggests alteration), and a high degree of translucency. Gem-like olivines 2–3 mm in diameter from the Esquel and Imilac pallasites, sampled >5 mm from the meteorite edge and several millimeters from the metal-olivine contact were found to have recoverable natural remanent magnetization (NRM) that was replicable within and between meteorite samples (2 from each meteorite). The success rate from the sampled olivines was 50% if the NRM was of order  $10^{-9}$  to  $10^{-10}$  A m<sup>2</sup> (only 15% of specimens analyzed). We therefore also preferentially selected samples with NRM moments of this magnitude.

The sample of Springwater from the Harvard Museum of Natural History (SWH) was a large slab (weight ~ 250 g, thickness ~ 1 cm) (Figure S5a). A small (~5 cm diameter) section was removed from one corner of the slab using an Buehler IsoMet® low speed saw (Figure S5b). All further sampling was carried out using a Well precision diamond wire saw at the MIT Paleomagnetism Laboratory. Cutting took place in a magnetically shielded clean room (DC field <200 nT), and the saw was thoroughly cleaned between sampling. Mutually oriented samples with a diameter of ~1–5 mm were prepared (Figure S5c). Samples were photo-

graphed before and after cutting in order to maintain orientation. Samples were mounted on 2.5-cm-diameter quartz glass disks using a minimal quantity of cyanoacrylate cement (Figure S5d). Quartz disks were cleaned using acetone to remove any contamination and alternating field (AF) demagnetized until they had a moment  $<1 \times 10^{-11} \text{ Am}^2$ .

A second piece of the Springwater sample from the Harvard Museum of Natural History (SWR) was removed using an ASC Scientific Dual Bladed Rock Saw. Samples were polished using  $1 \mu\text{m}$  Buehler alumina powder to remove the thin layer of epoxy protecting the sample surface. Olivines were then extracted using a small copper hammer and chisel at the Rochester Paleomagnetism and Rock Magnetism Laboratory. The boundary between each olivine and the FeNi matrix was gently tapped until the olivine “popped” out (Figure S6a). Given the considerable time needed to prepare oriented specimens following methods of Tarduno et al. (2012), unoriented samples were prepared for analysis. Extracted olivines were subsequently soaked in 1 molar HCl acid for  $\sim 12$  h to remove any surface contamination (Figure S6b). The NRM of olivine samples dropped by up to 2 orders of magnitude after acid treatment due to removal of alteration at the olivine-metal contact. Once the olivines had been soaked in acid, they were washed in deionized water and examined using a reflected light microscope. Any further obvious surface contamination was removed using a hand-held Dremmel drill. Samples were then mounted in a  $1\text{-mm}^3$ -fused quartz box, the magnetic moment of which was measured prior to mounting (Figure S6c). Where possible, samples were wedged in the box with no adhesion, but otherwise either a small amount of demagnetized OMEGA® cement or sodium silicate was used to fix the sample in place.

### 2.2.2. Alternating Field Demagnetization

Experiments were carried out on subsamples of Springwater (SW and SWH) and Imilac (IM) at the MIT Paleomagnetic Laboratory using a 2G Enterprises superconducting rock magnetometer. The magnetometer is shielded within a room made of permalloy and the ambient field is  $<200$  nT for DC fields and  $<40$  nT for AC fields. NRMs were removed by three axis AF demagnetization in steps of 0.5 mT up to 25 mT, followed by steps of 1 mT up to 95 mT and then steps of 1.5 mT up to 145 mT. The magnetic moment was measured after each AF step and the three orthogonal measurements then averaged to correct for any gyroscopic remanent magnetization (Garrick-Bethell et al., 2009; Tikoo et al., 2012). Two samples (SW1Aa and SW3Bb) were further demagnetized up to 420 mT in steps of 7.5 mT to test for higher coercivity components.

Paleointensity estimates were made by comparing the demagnetization of an NRM to either that of an anhysteretic remanent magnetization (ARM) or an isothermal remanent magnetization (IRM). Samples were given ARMs of 50, 100, and  $300 \mu\text{T}$  in an AC field of 260 mT and subsequently AF demagnetized up to 145 mT. Paleointensity estimates were calculated for high coercivity ( $>5$  mT) components (Figure S9a). The TRM equivalent paleointensity was calculated using

$$I_{ARM} = \frac{\Delta NRM}{\Delta ARM} \cdot \frac{B_{lab}}{f} \quad (5)$$

where  $\Delta NRM$  and  $\Delta ARM$  are the change in NRM and ARM between demagnetization steps.  $B_{lab}$  is the DC bias field and  $f$  is the TRM/ARM ratio which is taken to be  $f = 1.34$  because the paleomagnetic carriers in pallasite olivines are FeNi metal (Gattacceca & Rochette, 2004; Stephenson & Collinson, 1974; Tikoo et al., 2014).

TRM equivalent paleointensities were also determined by comparing AF demagnetization of the NRM to that of a 400 mT IRM for samples SW1Aa, SW1Ab, and SWH1frag. Paleointensities were determined using

$$I_{IRM} = \frac{\Delta NRM}{\Delta IRM} \cdot a \quad (6)$$

where  $\Delta NRM$  and  $\Delta IRM$  are the change in ARM and IRM between demagnetization steps, and  $a \sim 3,000 \mu\text{T}$  is a calibration constant, inversely proportional to the TRM/IRM ratio (Gattacceca & Rochette, 2004; Stephenson & Collinson, 1974). It should be noted that this calibration was measured for magnetite, although a similar trend has been observed for FeNi carriers (Fuller & Cisowski, 1989). The uncertainty in paleointensities estimated using this method may be large depending on the exact composition of FeNi carriers and grain size, as well as more fundamental questions of whether demagnetization characteristics

of TRM (unblocking temperatures) are adequately represented by ARM or IRM demagnetizations (which reflect magnetic coercivities). We therefore only use calculated paleointensities to assess whether samples acquired remanence in the presence or absence of a dynamo field.

### 2.2.3. Controlled Atmosphere IZZI Thellier–Thellier Experiment

Samples of Springwater (SWH) and Imilac (IM) were heated in a ASC Scientific TS-48SC thermal demagnetization oven (internal field <20 nT) in the MIT Paleomagnetic Laboratory. Samples were heated in a controlled H<sub>2</sub>–CO<sub>2</sub> atmosphere as described by Suavet et al. (2014). Samples were held at an oxygen fugacity of IW-2 where IW is the iron-wüstite buffer (Brett & Sato, 1984; Holmes & Arculus, 1982) using H<sub>2</sub>–CO<sub>2</sub> gas mixing. We followed the in-field, zero-field, zero-field, in-field (IZZI) protocol (Tauxe & Staudigel, 2004) and heated samples in steps of 25°C–50°C from 100°C to 500°C. Samples were held at each temperature for 20 min and took ~10–20 min to reach temperature, and <30 min to cool back to room temperature. Partial thermal remanent magnetization (pTRM) checks (Coe et al., 1978) were carried out at 150°C, 250°C, 325°C, and 400°C. For in-field and pTRM check steps, an applied laboratory field of 100 μT was used.

### 2.2.4. Laser Heated IZZI Thellier–Thellier Experiment

Samples of Springwater (SWR) were heated using a CO<sub>2</sub> laser in the University of Rochester Paleomagnetism and Rock Magnetism Laboratory in a three-layered shielded room with an ambient field of <200 nT. The power of the laser was calibrated to temperature using a thermocouple before measuring the samples. Each heating step took <5 min. Approximately 90 s were needed to reach temperature, and the temperature was held for 90 s. The “cooling time” before measurement was 90–120 s, but because of the very small thermal mass of the sample, cooling from high temperature occurs much more rapidly than this duration (O’Brien et al., 2020). Samples were heated and cooled in a magnetically shielded tube. The tube contained a coil so that laboratory fields could also be applied during heating. Both Thellier–Thellier experiments following the IZZI protocol and thermal demagnetization experiments in the absence of a laboratory field were conducted (Tarduno et al., 2012; Tauxe & Staudigel, 2004). All experiments were conducted using the small-bore (6.3 mm) ultra-high-sensitive three-component DC WSGI SQUID magnetometer. An applied laboratory field of 60 μT was used for in-field steps.

Samples were initially heated in three large temperature steps to 100°C, 210°C, and 290°C to minimize heating times and the chance of alteration at low temperature steps. Between 300°C and 700°C samples were heated in temperature steps of 10°C–20°C.

## 2.3. Asteroid Thermal Modeling

We follow a similar approach to Bryson et al. (2015) and assume that the pallasite parent body is spherically symmetric and cools via conduction alone. For the thermal evolution of the mantle, we iteratively solve

$$T_r^t = \kappa \delta t \left( \frac{1}{r \delta r} (T_{r+\delta r}^{t-\delta t} - T_{r-\delta r}^{t-\delta t}) + \frac{1}{\delta r^2} (T_{r+\delta r}^{t-\delta t} - 2T_r^{t-\delta t} + T_{r-\delta r}^{t-\delta t}) \right) + T_r^{t-\delta t} \quad (7)$$

where  $r$  is the radial distance from the center of the body,  $\delta r$  is the incremental distance which we set as 1 km,  $t$  is time since accretion,  $\delta t$  is the incremental time step,  $T_r^t$  is the temperature of the body at a given radial distance and time, and  $\kappa$  is the mantle thermal diffusivity. The surface temperature is fixed at 250 K, and the entire asteroid initially has a temperature of 1,600 K, which is approximately the silicate solidus. A summary of the parameters used in our calculations is given in Table 2.

### 2.3.1. Outward Growth of a Solid Inner Core

For nucleation and growth of a solid inner core, we assume the core is isothermal throughout asteroid cooling. For each time step, the entire core cools by

$$\Delta T = \frac{3k_m \left. \frac{\delta T}{\delta r} \right|_{r_c} \delta t}{\rho_c C_p r_c} \quad (8)$$

**Table 2**  
A Summary of the Parameter Values Used in Thermal and Dynamo Calculations

Symbol	Definition	Value	Units	Reference
$\delta t$	Time step	$2 \times 10^{11}$	s	Bryson et al. (2015)
$\delta r$	Incremental radius	1,000	m	Bryson et al. (2015)
$\Delta$	Relative slope of solidus versus adiabat	1.2		Nimmo (2009)
$\alpha$	Thermal expansivity	$9.2 \times 10^{-5}$	$\text{K}^{-1}$	Nimmo (2009)
$\Omega$	Rotational frequency	$4 \times 10^{-4}$	$\text{s}^{-1}$	Hanuš et al. (2013); Bryson et al. (2015)
$\rho_c$	Core density	7,019	$\text{kg m}^{-3}$	Nimmo (2009)
$C_p$	Specific heat capacity	835	$\text{J kg}^{-1} \text{K}^{-1}$	Nimmo (2009)
$\Phi_v$	Ohmic dissipation	0.2–2.0	$\text{W K}^{-1} \text{m}^{-3}$	Nimmo (2009)
$G$	Gravitational constant	$6.67 \times 10^{-11}$	$\text{m}^3 \text{kg}^{-1} \text{s}^{-2}$	
$f_i$	Fraction of inner-boundary related buoyancy	0.5		Aubert et al. (2009)
$\mu$	Magnetic permeability	$4\pi \times 10^{-7}$	$\text{H m}^{-1}$	
$f_{ohm}$	Fraction of ohmic dissipation	1		Aubert et al. (2009)
$f_{dip}$	Dipolar component	0.14		Evans et al. (2018)
$c$	Constant of proportionality	0.63		Evans et al. (2018)
$\kappa$	Mantle diffusivity	$5 \times 10^{-7}$	$\text{m}^2 \text{s}^{-1}$	Bryson et al. (2015)
$k_m$	Mantle thermal conductivity	3	$\text{W m}^{-1} \text{K}^{-1}$	Bryson et al. (2015)
$k_c$	Core thermal conductivity	30	$\text{W m}^{-1} \text{K}^{-1}$	Nimmo (2009)
$c_1$	Scaling prefactor	1.65		Aubert et al. (2009)
$F$	Efficiency factor	0.05		Evans et al. (2018)

where  $k_m$  is the mantle thermal conductivity,  $\rho_c$  is the core density,  $C_p$  is the core heat capacity, and  $r_c$  is the core radius. We allow the core radius to vary from 40% to 60% of the parent body radius.

To model the concentric outward growth of the solid inner core, we follow the model described by Nimmo (2009). The inner core spontaneously nucleates with a radius of 1 km. Its subsequent growth is given by

$$\frac{\delta r_i}{\delta t} \approx \frac{D^2}{2T_c f r_c (\Delta - 1)} \frac{\delta T_c}{\delta t} \quad (9)$$

where  $D = \sqrt{\frac{3C_p}{2\pi\alpha\rho_c G}}$  and is the scale height of convection,  $\alpha$  is the thermal expansivity, and  $G$  is the gravitational constant,  $T_c$  is the temperature at the core–mantle boundary,  $f$  is the fraction of core that has solidified, where  $r_i = f r_c$  and  $\Delta = \frac{\delta T_m}{\delta P} \frac{\rho C_p}{\alpha T_i}$  is the relative slope of the solidus to the adiabat ( $\Delta > 1$  for inner core solidification). The cooling rate is taken from our thermal model for the pallasite parent body at the core–mantle boundary. When the core cools to the FeS eutectic (1,200 K) it remains isothermal until it is entirely solid. We terminate the model when the core is fully solidified, dictated by the total heat extracted across the core–mantle boundary equaling the latent heat of the core:

$$Q_{cmb} = 4\pi r_c^2 k_m \left. \frac{\delta T}{\delta r} \right|_{r_c} = \frac{4}{3} \pi r_c^3 \rho_c L_c \quad (10)$$

where  $Q_{cmb}$  is the core–mantle boundary heat flux and  $L_c$  is the latent heat of core solidification.  $\left. \frac{\delta T}{\delta r} \right|_{r_c}$  was calculated at each time step by taking the difference between the temperature directly above and below the core–mantle boundary. The extracted heat is summed over each subsequent time step until it exceeds the latent heat of the core.

### 2.3.2. Inward Growth of a Solid Outer Core

For concentric inward growth of the core beginning at the core–mantle boundary, we follow the approach of Scheinberg et al. (2016). We assume that the core begins to solidify at the core–mantle boundary when its liquidus temperature is reached. The core is held at the liquidus temperature until a shell ( $r_{shell}$ ) of 1 km thickness has solidified at the top of the core. The subsequent thermal evolution of the core is governed by

$$Q_{ocb} = \frac{4}{3}\pi \left( r_{oc}^3 - (r_{oc} - r_{shell})^3 \right) \rho_c L_c \quad (11)$$

where  $Q_{ocb}$  is the heat flux across and  $r_{oc}$  is the radius of the solid-outer-core liquid-inner-core boundary. The solid outer core and the mantle continue to lose heat via conduction, driving further solidification of the core. When the liquid portion of the core reaches the eutectic temperature (1,200 K), this liquid is held at the eutectic temperature throughout the remaining solidification. Solidification is complete when the cumulative heat flux exceeds the latent heat of the core:

$$Q_{ocb} = \frac{4}{3}\pi r_{ic}^3 \rho_c L_c \quad (12)$$

### 2.3.3. The Influence of Sulfur Content on Core Solidification

The core begins to solidify when it reaches the FeS liquidus temperature, which we vary from 1,200 to 1,590 K corresponding to 18–31 wt% S (Ehlers, 1972). We assume that the core is entirely liquid and the mantle is solid when the asteroid differentiates, and therefore the highest liquidus temperature of the core must be below the silicate solidus temperature (1,600 K), which corresponds to 18 wt% S. It is assumed that all the sulfur remains in the liquid part of the core and the sulfur content of the liquid core increases by

$$X_{S_{liq}} = \frac{r_c^3}{r_{liq}^3} X_{S_o} \quad (13)$$

where  $X_{S_{liq}}$  is the sulfur content of the liquid part of the core,  $X_{S_o}$  is the initial sulfur content of the core, and  $r_{liq}$  is the radius of the liquid part of the core. This causes a decrease in the liquidus temperature as core solidification progresses until the FeS eutectic is reached.

### 2.3.4. The Depth of the Pallasites Within the Parent Body

The depths of the pallasites within the parent body were calculated based on their cooling rates (Table 4) which were determined at a temperature of 800 K (Yang et al., 2010). We use the 800 K isotherm to find the depth at which each of these cooling rates is met (Bryson et al., 2015). These depths were then interpolated along the 593 K isotherm to find the time at which each pallasite formed tetrataenite, which also corresponds to the time of remanence acquisition. For the pallasite olivines measured by Tarduno et al. (2012), the depths of the Imilac and Esquel pallasites were interpolated along the 633 K contour, which corresponds to the thermal blocking temperature for taenite with 50–55 wt% Ni.

## 2.4. Asteroid Magnetic Field Generation

### 2.4.1. A Dynamo Driven by Inner Core Growth

For outward solidification of a core, the mechanism of dynamo generation via compositional convection is well understood. For this mode of core solidification, we calculated the temporal evolution of a dynamo for each of our thermal models. The buoyancy flux,  $Q_b$ , generated by core solidification was calculated following Christensen and Aubert (2006) and Aubert et al. (2009):

$$Q_b = \frac{2\pi r_c f \Delta \rho D^2}{T_c (\Delta - 1)} \frac{\delta T_c}{\delta t} \quad (14)$$

which can be used to calculate the flux-based Rayleigh number:

$$Ra_Q = \frac{G Q_b}{4\pi \Omega^3 d^4} \quad (15)$$

where  $\Omega$  is the rotational frequency of the planetesimal and  $d$  is the thickness of the molten part of the core. We assume a fairly rapid rotational frequency consistent with that observed for the asteroid (16) Psyche (Hanuš et al. 2013 and Table 2). The power per unit volume,  $P$ , of the resulting dynamo is proportional to the Rayleigh number where  $P = \gamma Ra_Q$  and

$$\gamma = \frac{3(r_c - r_i c)^2}{2(r_c^3 - r_i c^3)r_c} \left[ f_i \left( \frac{3 r_c^5 - r_i c^5}{5 r_c^3 - r_i c^3} \right) + 1 - f_i \left( r_c^2 - \frac{3 r_c^5 - r_i c^5}{5 r_c^3 - r_i c^3} \right) \right] \quad (16)$$

where  $f_i$  is the fraction of inner-boundary originated buoyancy which is taken to be  $\sim 0.5$ .

The strength of the magnetic field generated at the core–mantle boundary ( $B_{cmb}$ ) is given by

$$B_{cmb} = c_1 f_{ohm}^{0.5} P^{0.34} (\rho \mu)^{0.5} \Omega D \quad (17)$$

where  $c_1$  is a scaling prefactor (Aubert et al., 2009),  $\rho$  is the density of the fluid part of the core,  $\mu$  is magnetic permeability, and  $f_{ohm}$  is the fraction of ohmic dissipation. Assuming a planetocentric dipolar field, the strength of the magnetic field at the depth of the pallasites is given by

$$B_{pal} = \left( \frac{r_c}{r_{pal}} \right)^3 B_{cmb} \quad (18)$$

where  $r_{pal}$  is the distance from the center of the parent body to the pallasite depth (constrained by our thermal model).

#### 2.4.2. Maximum Magnetic Field Generation Potential

Since dynamo generation in cores undergoing inward solidification is poorly understood and an area of active research, we do not attempt to model dynamo behavior for this scenario. In order to compare inward versus outward core solidification without invoking a dynamo generation mechanism, we calculated the maximum magnetic field intensity the pallasites could have experienced following the approach of Evans et al. (2018). We consider all energy sources available to the core: gravitational energy ( $E_G$ ), thermal energy ( $E_T$ ), latent energy ( $E_L$ ), and radioactive energy ( $E_R$ ). Given the small size of the pallasite parent body and the uranium content of the pallasites (85 ppb; Crozaz et al., 1982), we find that radioactive energy is negligible. We also find that thermal and gravitational energy are negligible compared to latent energy:

$$E_L = \frac{4}{3} \pi \rho_c (r_c^3 - r_{ic}^3) L_c \quad (19)$$

The maximum average intensity of the magnetic field ( $B_{max}$ ) at the depth of the pallasites is given by

$$B_{max} \approx f_{dip} \left( \frac{r_c}{r_{pal}} \right)^3 \sqrt{2 \mu c f_{ohm} \rho_c^{-\frac{1}{3}} (F Q_{cmb})^{\frac{1}{3}}} \quad (20)$$

where  $Q_{cmb} = \frac{E_L(t)}{A_c \Delta t_c}$  where  $A_c$  is the surface area of the core and  $\Delta t_c$  is the length of time over which the dynamo is active,  $f_{dip}$  is the dipolar fraction of the magnetic field,  $c$  is a constant of proportionality, and  $F$  is an efficiency factor (Evans et al., 2018).

### 3. Results

#### 3.1. Cloudy Zone Paleointensities

Histograms of XMCD intensity were calculated for the region of cloudy zone adjacent to the tetraenaite rim (Figure 1). The mean XMCD intensity was calculated from the histograms of pixel intensity for eight regions of cloudy zone for each rotation (Table S2). Paleointensities were determined using Equations 1–3 and we found the Springwater cloudy zone records a unidirectional paleointensity of  $22 \pm 8 \mu\text{T}$  (Figure 2).

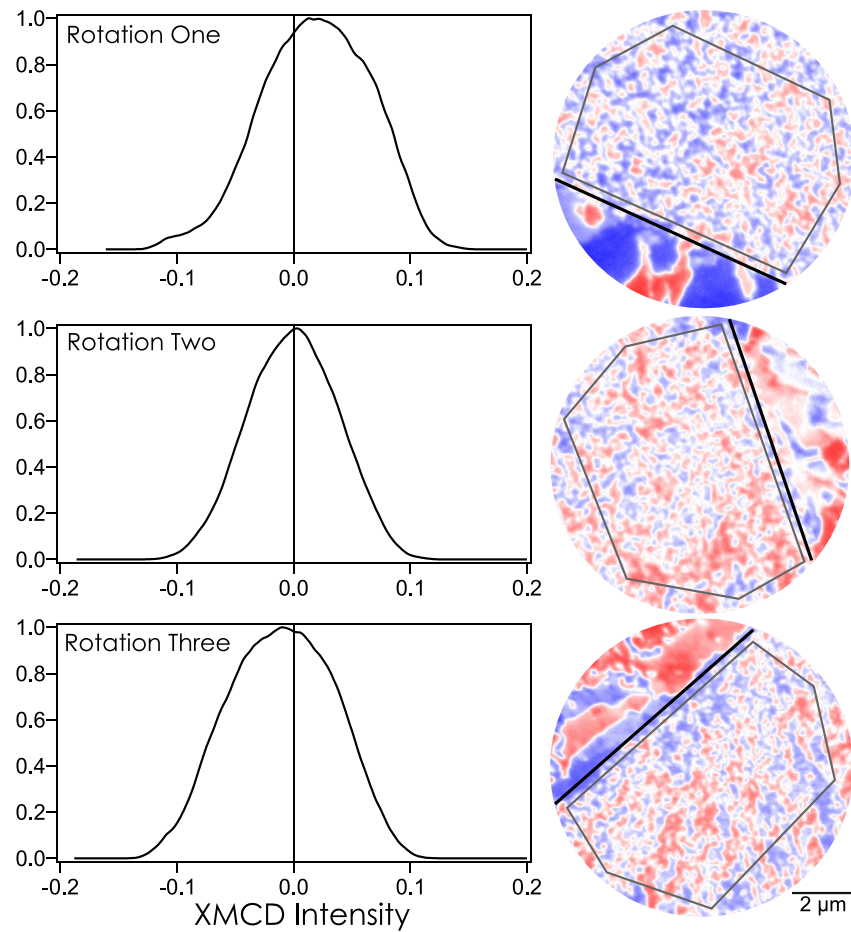


**Figure 1.** Histograms of pixel intensity for the coarse cloudy zone, and an example of an XMCD image for each rotation. All histograms are corrected using corrections calculated from Equation S1. XMCD, X-ray magnetic circular dichroism.

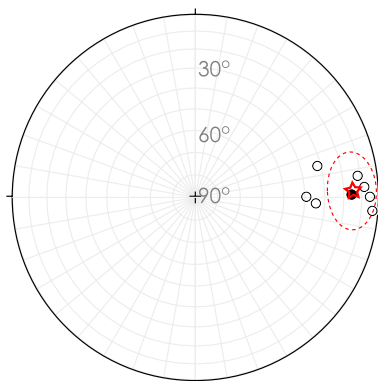


**Figure 2.** Equal area polar stereonet projection showing the direction of magnetization for the eight analyzed regions of cloudy zone in Springwater imaged using X-PEEM. The results show that magnetization is unidirectional. The mean direction is shown by the red star and the 95% confidence interval on the direction by the dashed red circle. Dashed and open symbols are upper-hemisphere projections; solid symbols are lower-hemisphere projections. X-PEEM, X-ray photoemission electron microscopy.

We have also reassessed previous studies on the Imilac, Esquel, Brenham, and Marjalahti pallasites and updated their paleointensities and corresponding uncertainties to reflect their analysis for only a single rotation (Bryson et al., 2015; Nichols et al., 2016). The original paleointensity estimates were improved upon by Maurel et al. (2019) after the size of the islands in the cloudy zone at the point of remanence acquisition was established to have been  $\sim 78\%$  of their present-day diameter. Here, we estimate the upper limit on these revised paleointensities to 95% confidence (Table 3).

### 3.2. Magnetic Behavior of Olivine Inclusions

#### 3.2.1. Alternating Field Demagnetization

We carried out NRM AF demagnetization of 3 subsamples of Imilac and 11 subsamples of Springwater (Table S6). We found that the three subsamples of Springwater taken from the AMNH sample (SW) have been overprinted by a strong IRM, most likely from a collector's hand magnet (Figure S8) and were therefore discounted from our assessment of the NRMs. For the other subsamples (IM and SWH) low ( $< 7$  mT)

**Table 3**  
A Summary of the Paleointensity Estimates Calculated From the Cloudy Zone for Each of the Main Group Pallasites

Meteorite	Original paleointensity estimate ( $\mu\text{T}$ )	Revised paleointensity estimate ( $\mu\text{T}$ ) <sup>a</sup>	Maximum paleointensity estimate ( $\mu\text{T}$ ) <sup>b</sup>
Marjalahti	$<7^c$	0.2	3
Brenham	$<7^c$	0.3	5
Springwater	$22 \pm 8^b$	–	–
Imilac	$119 \pm 12^d$	$6.8 \pm 2.0$	$80 \pm 15$
Esquel	$84 \pm 14^d$	$4.8 \pm 1.5$	$64 \pm 15$

Note. The first column lists the pallasite measured. The second column lists the original measured paleointensities assuming islands acquire remanence at 30% of their present-day diameter. The third column lists the revised paleointensity estimates based on improved understanding of cloudy zone island remanence acquisition at ~78% of their present diameter. The fourth column lists upper estimates on X-PEEM intensities to 95% confidence by taking into account the uncertainty in measurement direction because they were only imaged in one orientation.

<sup>a</sup>Maurel et al. (2019). <sup>b</sup>This study. <sup>c</sup>Nichols et al. (2016). <sup>d</sup>Bryson et al. (2015).

and high coercivity (7–35 mT) components were identified. High coercivity components were forced through the origin. The high coercivity component is poorly defined for many samples, highlighted by high maximum angular deviation (MAD) values ( $>20^\circ$ ). The directions of the low and high coercivity components were plotted on a stereonet for each set of oriented subsamples from Imilac and Springwater (Figure 3). No evidence was found for a stable direction for low or high coercivity components in either sample, suggesting that no primary NRM is recoverable.

We assessed the fidelity of Springwater olivines as remanence carriers by comparing NRM demagnetization to laboratory applied ARM and IRM demagnetization (Table S5). To quantify the fidelity, we followed the approach of Tikoo et al. (2012) and Bryson et al. (2017). We consider:  $D'$ , the difference between the applied laboratory field and the retrieved paleointensity; and  $E$ , the error associated with the retrieved paleointensity compared to the applied laboratory field, where

$$D' \equiv \frac{I - L}{L} \cdot 100\% \quad (21)$$

and

$$E \equiv \frac{W}{L} \cdot 100\% \quad (22)$$

where  $L$  is the laboratory field,  $I$  is the retrieved paleointensity, and  $W$  is the 95% confidence interval on the recovered paleointensity.  $D'$  and  $E$  were calculated for Springwater using both the ARM method (Equation 5 and Figure S9c) and the IRM method (Equation 6 and Figure S9d). Results are presented in Table S5. We consider generous acceptance criteria for reliable paleomagnetic recorders;  $-50\% > D' < 100\%$  and  $E < 100\%$  (Bryson et al., 2017). Figure 4 shows results of the fidelity tests, which do not reliably fall within the acceptance criteria suggesting these pallasite olivines are not robust paleomagnetic recorders of magnetic fields  $<225 \mu\text{T}$ , as estimated by ARM and IRM methods.

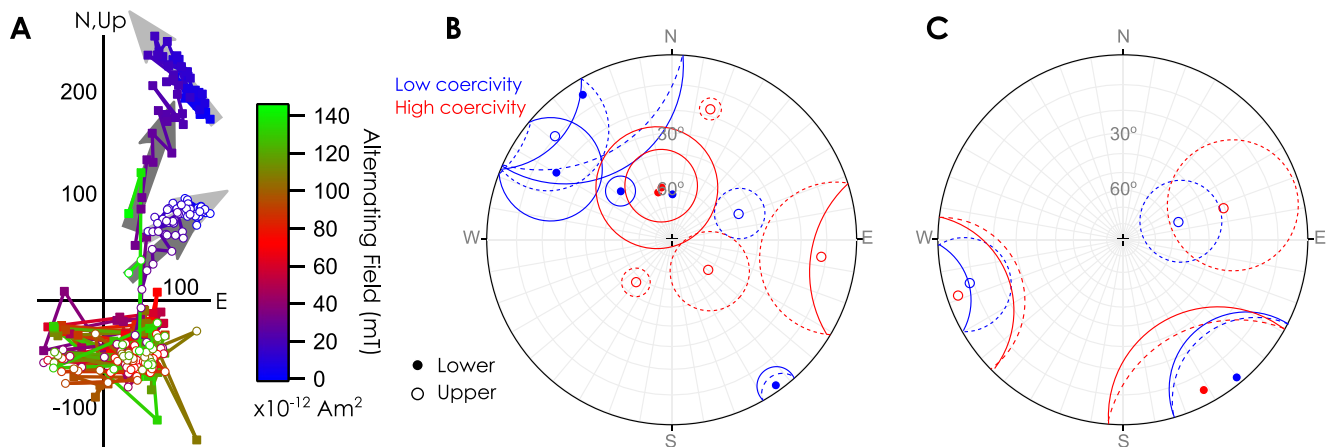


**Figure 3.** (a) Zijderveld plot for NRM demagnetization of subsample SWH1frag from a Springwater olivine. Closed squares show declination, open circles show inclination, and the color bar represents the strength of AF demagnetization. Low and high coercivity components are shown by the light and dark gray arrows, respectively. (b) Equal area stereographic projection of the NRM directions measured for Springwater (SWH). Blue and red circles denote the low and high coercivity components, respectively. Open circles are points in the upper hemisphere, while closed circles are points in the lower hemisphere. The surrounding circles are the  $\alpha_{95}$  for each component. (c) Equal area stereographic projection of the NRM directions measured for Imilac (IM). NRM, natural remanent magnetization; AF, alternating field.

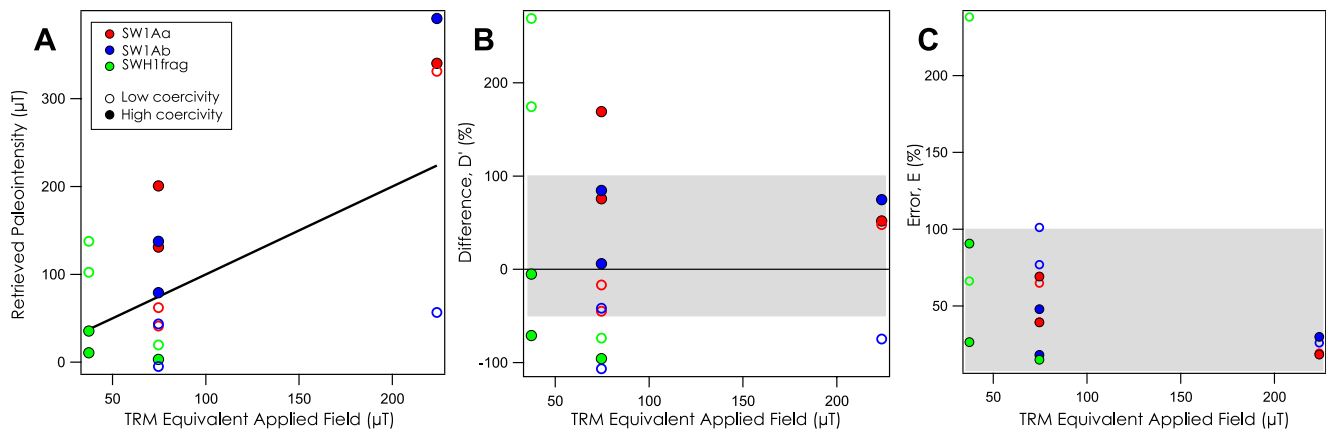


**Figure 4.** Fidelity tests for SW1Aa, SW1Ab, and SWH1frag are shown in red, blue, and green, respectively. Paleointensity estimates for low and high coercivity components are shown by open and closed circles, respectively. (a) The retrieved paleointensity versus applied field. The thick black line is a 1:1 relationship between the retrieved paleointensity and applied field. (b) The difference between the retrieved paleointensity and applied field. The gray box shows the region for which paleointensity estimates are acceptable within the arbitrary threshold. (c) The error on the retrieved paleointensity versus applied field. These values should be below the marked 100% threshold, as shown by the gray box.

### 3.2.2. Controlled-Atmosphere Thermal Demagnetization

We conducted controlled atmosphere IZZI Thellier–Thellier experiments on five subsamples of Springwater (SWH) and six subsamples of Imilac (Figures S17 and S16). In all cases, we found that pTRM checks failed at low temperatures (<250°C; Table S8). We found that following heating, nanoscale FeNi particles appeared to have grown along cracks in the olivine crystals (Figure S12). This is consistent with the observed change in the rock magnetic properties of the samples. After heating, the coercivity of the samples had increased (Figure S13) and the hysteresis loops indicate that magnetic carriers with ideal, single-domain characteristics had formed (Figure S15). Quantum diamond microscopy showed that the magnetic phases are concentrated along cracks; however, given that these were imaged after applying a saturating IRM of 300 mT, we cannot quantify their contribution to the measured NRM (Figure S14).

### 3.2.3. CO<sub>2</sub> Laser Thermal Demagnetization

IZZI Thellier–Thellier experiments were also conducted on two subsamples of Springwater (SWR) in air using a CO<sub>2</sub> laser. An origin-trending component was identified in subsample SWRTopD3 between 350°C and 500°C; however, pTRM checks failed at 305°C–320°C and therefore demagnetization was not continued to higher temperatures (Figure S18 and Table S9).

## 3.3. Thermal and Dynamo Model Results for the Pallasite Parent Body

Our experimental data are used to place two important constraints on the cooling model for the pallasite parent body. First, using previously measured X-PEEM images that demonstrated that Marjalahti and Brenham recorded a null field, we assume that these meteorites captured a magnetic field record prior to core solidification (Nichols et al., 2016). We assume that there was no driving force for a dynamo following early thermal convection, and prior to core solidification, which would initiate compositional convection (Bryson, Neufeld, et al., 2019; Elkins-Tanton et al., 2011). Second, Springwater, Imilac, and Esquel acquired paleointensities while a dynamo was active, most likely during core solidification. The model-derived timing of remanence acquisition for each pallasite is given in Table 4.

For inner core nucleation, we found the thermal evolution of parent bodies with a radius between 180 and 360 km was consistent with our experimental results (Figure 6a and Table S10). The parent body cannot have a radius <180 km because there is insufficient time for Springwater, Imilac, and Esquel to acquire remanence before the core is entirely solid. The upper limit on parent body size (360 km) is constrained by the sulfur content of the core; the liquidus temperature must be sufficiently high for core solidification to

**Table 4**  
Table Showing the Cooling Rates and Timing of Remanence Acquisition for Each Pallasite Studied Using Paleomagnetism

Pallasite	Cooling rate (°C Myr <sup>-1</sup> )	Inferred depth in parent body (km)	Inferred height above CMB (km)	Time of NRM (Myr after accretion)
Inner core nucleation				
Marjalahti	7.6 ± 0.6	22 ± 1.5	92 ± 20	92 ± 6
Brenham	6.6 ± 0.5	24 ± 1.5	90 ± 20	105 ± 5
Springwater	5.4 ± 0.5	27 ± 2	87 ± 20	129 ± 7
Imilac	4.3 ± 0.3	31 ± 2.5	83 ± 20	163 ± 7
Esquel	3.3 ± 0.6	35 ± 4	79 ± 20	209 ± 8
Outer core nucleation				
Marjalahti	7.6 ± 0.6	21 ± 1	39 ± 5	102 ± 7
Brenham	6.6 ± 0.5	22 ± 1	37 ± 4	119 ± 11
Springwater	5.4 ± 0.5	24 ± 2	36 ± 4	135 ± 6
Imilac	4.3 ± 0.3	26 ± 3	33 ± 3	153 ± 4
Esquel	3.3 ± 0.6	29 ± 5	30 ± 1	176 ± 14

*Note.* The first column is the name of the studied pallasite. The second column is the cooling rate of the pallasite (Yang et al., 2010). The third column is the inferred depth of the pallasite within the parent body. The fourth column is the inferred height of the pallasite above the core-mantle boundary. The fifth column is the inferred time of remanence acquisition; the cloudy zone acquires remanence upon cooling through 320°C.

begin before Springwater acquired its remanence. The FeS liquidus exceeds 1,600 K (the silicate solidus) when  $S < 18$  wt% (Ehlers, 1972). Since we assume both the metal and silicate components of the parent body are entirely liquid upon accretion to ensure complete differentiation sulfur contents below 18 wt% are not considered.

For outer core nucleation, all the cooling model solutions for inner core nucleation remain valid; however, core solidification extends over significantly longer time scales (Figure 5b). We found that the minimum mantle thickness was also smaller for inward core solidification compared to outward core solidification for similar sized cores (Figure 7).

For each plausible cooling model solution, we calculated the evolution of a dynamo driven by inner core solidification. The resulting dynamo model was compared to our experimental data (Figure 6). We found that for dynamo evolution to be consistent with our measured paleointensities, relatively long core solidification times (>180 Myr) and large cores (>170 km) are required.

Using our planetesimal models for both inward and outward core nucleation, we calculated the maximum intensity that the dynamo could have generated, assuming it was continuously active between the Springwater and Esquel cloudy zones cooling through the tetrataenite ordering temperature. The maximum intensities generated for inward and outward core solidification were 80 and 72  $\mu$ T, respectively. Our results suggest that a planetesimal with a large core and thin mantle has sufficient energy to generate the observed high paleomagnetic field intensities (Figure 7).

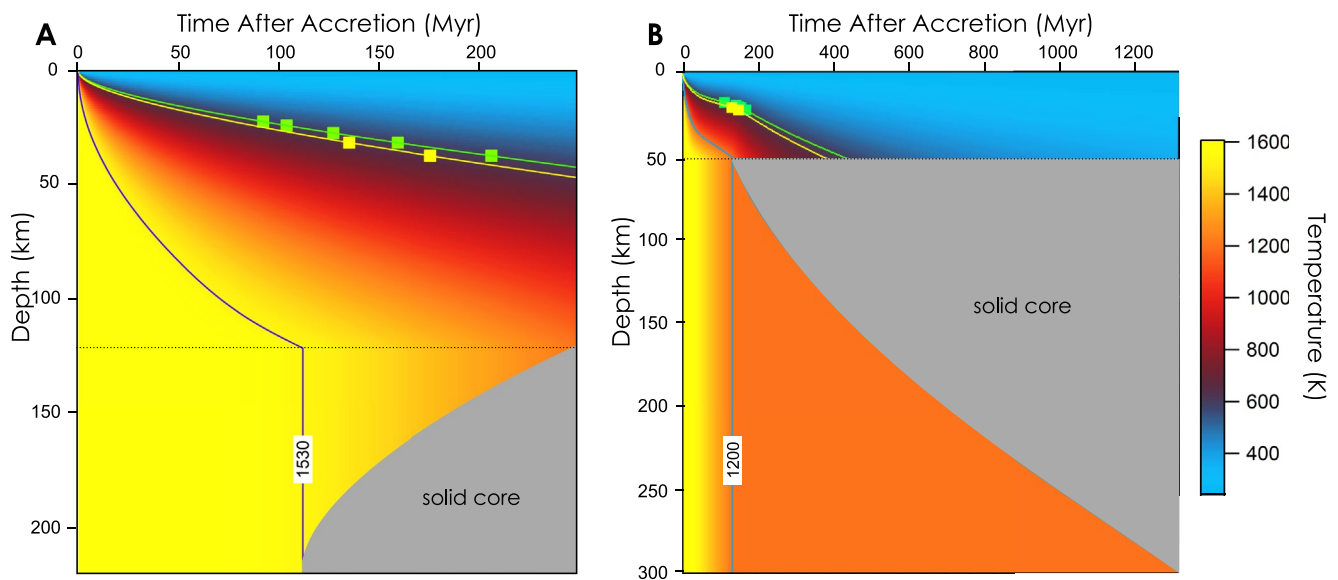


**Figure 5.** Thermal evolution models for planetesimals with outward and inward core solidification. The green line is the 593 K contour, which is the temperature at which the cloudy zone acquires remanence. The green squares represent the timing of remanence acquisition for the Marjalahti, Brenham, Springwater, Imilac, and Esquel cloudy zones. The yellow line is the 633 K contour, which is the temperature at which the pallasite olivines acquire remanence (Tarduno et al., 2012). The yellow squares are for the Imilac and Esquel olivines. The gray region shows the solid part of the core. (a) Thermal model for outward core solidification within a planetesimal of radius 220 km with a core radius of 100 km. The purple line is the 1,530 K contour, which is the liquidus of FeS with a composition of 23 wt% S. (b) Thermal model for inward core solidification within a planetesimal of radius 300 km with a core radius of 250 km. The blue line is the 1,200 K contour, which is the liquidus of FeS with a composition of 31 wt% S.

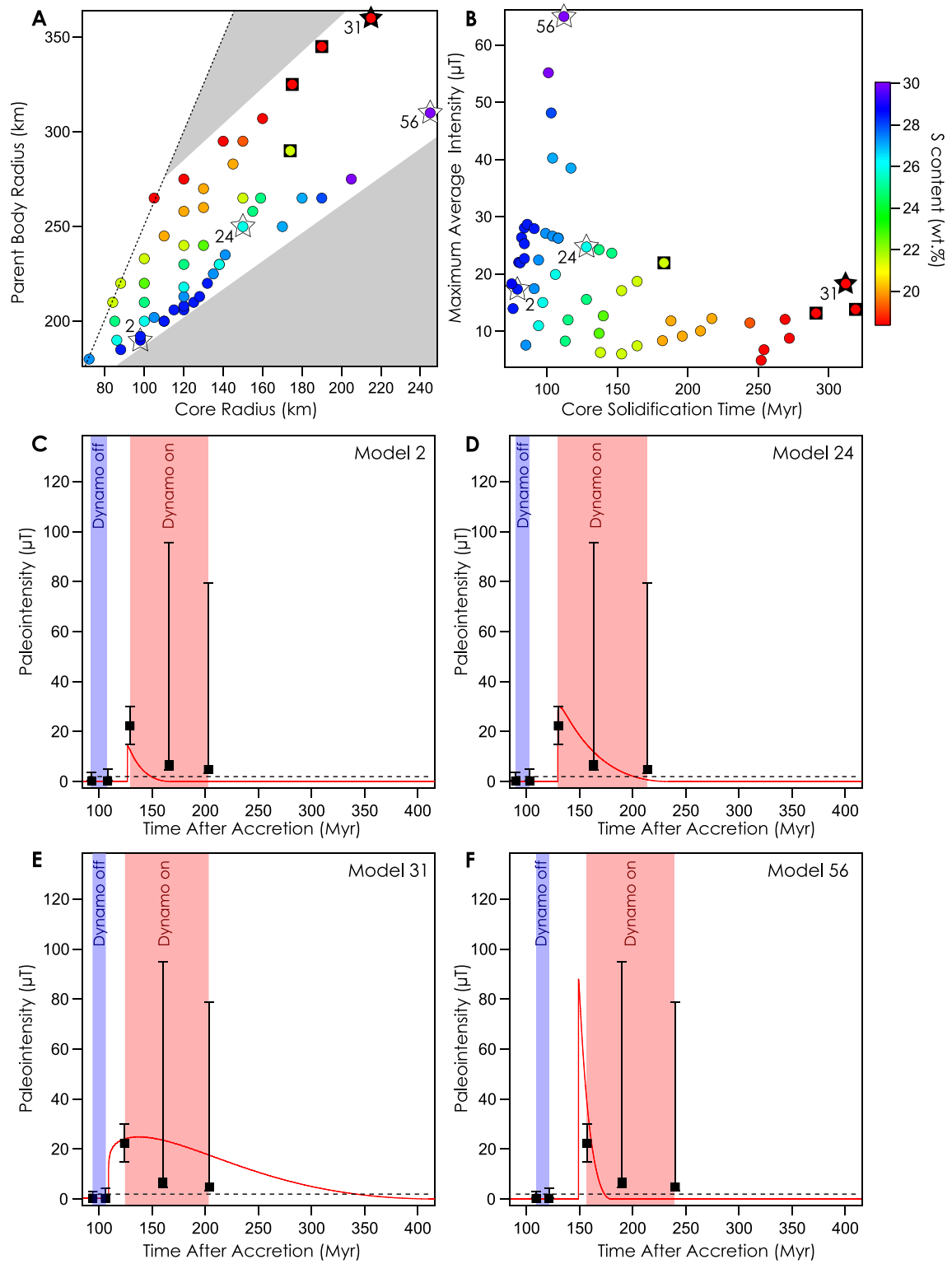
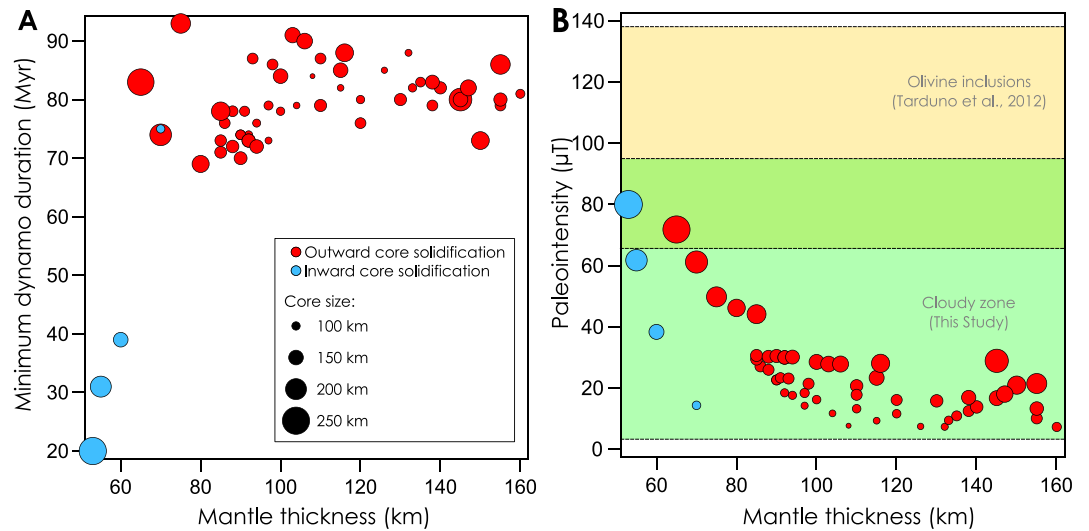


Figure 6



**Figure 7.** The effect of mantle thickness on dynamo duration and mean dynamo intensity. Red points are for our thermal models for outward core solidification. Blue points are for our thermal models for inward core solidification. The size of the point represents the size of the planetesimal core. (a) Minimum dynamo duration (the time between Springwater and Esquel acquiring remanence) as a function of mantle thickness. For outward solidification, there is little dependence on mantle thickness or core size. For inward core solidification, the dynamo duration depends strongly on mantle thickness. (b) The yellow region represents the paleointensity results reported by Tarduno et al. (2012) for Imilac and Esquel. The green region represents the paleointensities reported here from X-PEEM studies of Springwater, Imilac, and Esquel. The yellow-green region shows where independent paleointensity estimates overlap. To generate paleointensities consistent with both sets of observations, the pallasite parent body must have had a large core and thin mantle, regardless of the direction of core solidification. X-PEEM, X-ray photoemission electron microscopy.

## 4. Discussion

### 4.1. Pallasites as Paleomagnetic Recorders

In recent years, significant progress has been made to understand how remanence is acquired by the cloudy zone and to improve methods for retrieving a reliable, quantified paleointensity. The first studies on the paleomagnetism of the cloudy zone in pallasites (Bryson et al., 2015; Nichols et al., 2016) assumed that the cloudy zone could record time-resolved information, with the oldest record in the coarsest cloudy zone immediately adjacent to the tetrataenite rim, and the youngest record in the fine cloudy zone, furthest from the tetrataenite rim. Einsle et al. (2018) subsequently showed that a significant portion of the cloudy zone acquires remanence simultaneously upon cooling through 320°C, when the islands order to tetrataenite. The diameter of the islands at the time of tetrataenite ordering was also found to be much larger (92–122 nm; Maurel et al., 2019) than previously assumed (35–45 nm; Bryson et al., 2015; Nichols et al., 2016), lowering the paleointensity estimates for Marjalahti, Brenham, Imilac, and Esquel (Table 3; Maurel et al., 2019).

**Figure 6.** Thermal and dynamo model solutions. (a) The parent body sizes and sulfur compositions that produced cooling models consistent with our experimental data. We only consider core sizes between >40% of the parent body radius, represented by the black dashed line. Gray regions represent parent body configurations inconsistent with our experimental data. The color of the points represent their sulfur content. Black squares represent cooling models which also generated a dynamo consistent with our experimental data. Four examples of dynamo model results are highlighted by stars. Closed and open stars are examples of dynamo models shown in that were (e) and were not (c, d, f) consistent with our experimental data. (b) The maximum intensity and core solidification time corresponding to each cooling model shown in (a). (c) Dynamo evolution due to inner core nucleation, for model 2 (Table S10). Black squares and vertical error bars are the measured paleointensities of the pallasite cloudy zones using X-PEEM. The relative timings of remanence acquisition are calculated from the cooling model. The red line shows the evolution of a dynamo driven by core solidification. The black dashed line shows the minimum paleointensity that can be attributed to an active dynamo. Model 2 is too weak to explain the measured paleointensities. The shaded regions represent experimental constraints on when there was no dynamo and the core was entirely liquid (blue region) and when there was an active dynamo and the core was solidifying (red region). (d) Model 24 does not sustain a dynamo for long enough to explain the measured paleointensities. (e) Model 31 matches the measured paleointensities. (f) Model 56 generates a dynamo which is too short and intense to explain the measured paleointensities. X-PEEM, X-ray photoemission electron microscopy.

The experimental method using X-PEEM to image the distribution of magnetization in the cloudy zone has also been improved. Previous studies imaged the distribution of magnetization in the cloudy zone in a single orientation (Bryson et al., 2015; Nichols et al., 2016). This does not allow the 3D vector of magnetization to be fully resolved. Therefore, only a minimum paleointensity estimate and minimal (constrained to within a hemisphere) directional information can be recovered. We imaged Springwater in three rotations, adopting the improved method outlined by Bryson et al. (2019). Therefore, the paleointensity and direction (relative to the sample) of magnetization in the Springwater pallasite have been fully resolved. We have also improved upon the paleointensity estimates for Marjalahti, Brenham, Imilac, and Esquel calculated by Maurel et al. (2019) by accounting for the fact these paleointensity estimates were only lower limits. We have calculated upper bounds on the true paleointensity and found that our results are consistent with the paleointensities reported for Imilac and Esquel olivines (Tarduno et al., 2012).

Given the developments in the understanding of cloudy zone paleomagnetism, we are now able to present the most detailed time-resolved record of paleointensities on the MG pallasite parent body. Further work is still required to understand the role of interactions between cloudy zone islands. However, since we have assumed no interaction, accounting for magnetostatic interactions between islands will only increase our paleointensity estimates (Dunlop & Ozdemir, 1997). Despite the significant uncertainty associated with some of the paleointensities, an increase in paleointensity over time—most likely triggered by the onset of dynamo activity—can be resolved and the implications of this record are considered in the following sections.

Single crystal thermal paleointensity methods applied to pallasite olivines are challenging because of the significant time needed in sample selection, preparation, and experiments, as well as the potential for thermal alteration. Using techniques previously developed at the University of Rochester (Tarduno et al., 2006), the time for conducting single crystal paleointensity studies typically spans multiple years, rather than the 2 weeks in which the laser-heated experiments discussed here were conducted at the University of Rochester. Additional experiments using AF and controlled-atmosphere heating techniques were conducted at MIT over 3 months. Our AF experiments demonstrated the poor recording fidelity of pallasite olivines, which cannot reliably record paleointensities  $<225 \mu\text{T}$  using ARM and IRM methods. Controlled-atmosphere experiments were also unable to prevent olivine alteration. In contrast, some olivines can be cycled through multiple TRMs and show properties meeting Thellier's criteria (Tarduno et al., 2012). Springwater olivines are 18% fayalitic (Righter et al., 1990) and Imilac olivines are 12.3% fayalitic (Wasson & Choi, 2003) suggesting that they have an equivalent oxygen fugacity at high temperatures (Righter et al., 1990). However, experimental evidence suggests that pallasite fugacity can vary significantly (Brett & Sato, 1984; Holmes & Arculus, 1982). Given the rapid alteration of olivines at low temperatures ( $150^\circ\text{C}$ ), it appears that our samples were not in equilibrium with the controlled atmosphere. The growth of nanoscale FeNi particles may be indicative that the atmosphere (IW-2) was too reducing.

Previous studies (Tarduno & Cottrell, 2013; Tarduno et al., 2012) reported successful thermal demagnetization of olivines from the Imilac, Esquel, and Springwater pallasites. The method used for these studies involved heating samples with a  $\text{CO}_2$  laser in air with short heating and cooling times of a few minutes. The null success rate for our controlled-atmosphere thermal experiments is possibly attributed to the low number of samples measured (7 for Springwater [SWH] and 6 for Imilac). Similar unsuccessful results were reported by Tarduno et al. (2012) and further indicate that only some millimeter-sized pallasite olivines have inclusions from which paleointensities can be retrieved by heating. We suggest that at least twice as many specimens should be measured as studied here to obtain paleointensity values. This is supported by our identification of a stable remanence component in only one of our Springwater specimens, SWRTopD3 (Figure S18), which suggests preservation of magnetic minerals recording a primary magnetization. The experimental challenges encountered when measuring pallasite olivines highlight the benefits of studying the cloudy zone. Our X-PEEM technique does not require sample heating and therefore offers an effective approach for recovering paleointensities without risk of sample alteration. However, the availability of results from pallasite olivines is important in our following discussion because results obeying Thellier laws are independent of those acquired using X-PEEM and the fact that both yield results indicating a past magnetization gives us confidence in our further consideration of the interior dynamics and structure of the pallasite parent body.

#### 4.2. Time-Resolved Records of Magnetic Activity on the Main Group Pallasite Parent Body

We present a comprehensive time-resolved paleomagnetic record for the MG pallasite parent body. We have used these paleomagnetic observations to constrain the thermal evolution of the pallasite parent body following a similar approach to Tarduno et al. (2012) and Bryson et al. (2015). Assuming that the dynamo was driven by core solidification, Brenham and Marjalahti acquired a null remanence (or experienced magnetic field intensities too weak to attribute to an active dynamo) prior to the onset of solidification, while Springwater, Imilac, and Esquel acquired remanence while the core was still partially liquid consistent with predictions for asteroid dynamo behavior (Bryson et al., 2019). Previous studies only considered eutectic solidification of FeS at 1,200 K, corresponding to a sulfur content of 31 wt% (Bryson et al., 2019; Bryson et al., 2015; Tarduno et al., 2012). For solidification at the eutectic, we found that for parent bodies that were sufficiently small for Springwater to acquire remanence after the onset of core solidification, Esquel could not have acquired remanence before core solidification was complete. It should also be noted that eutectic solidification of the core will in fact not drive a thermochemical dynamo, although it is a reasonable approximation for considering the thermal evolution of a core. We therefore consider lower sulfur compositions in our planetary cooling model that correspond to higher FeS liquidus temperatures. The raised liquidus temperature causes core solidification to begin at earlier times and allows a thicker mantle, resulting in slower cooling and longer solidification times. By varying the sulfur content and core size, we found a range of plausible parent body sizes from 180 to 360 km radius, a larger upper limit than that reported by Bryson et al. (2015). We found that permissible parent body sizes increase with decreasing sulfur content and increasing core size (Figure 6).

#### 4.3. Implications for Core Crystallization and Dynamo Generation

We have considered both outward and inward core solidification for the pallasite parent body. In both cases, we assume concentric growth and do not account for the possibility of dendritic growth or other more exotic styles of crystallization (Scheinberg et al., 2016). Our models can therefore be considered as lower limits on the time of core solidification. This does not affect the implications of our results, which primarily depend on the core beginning to solidify between the times at which Brenham and Springwater acquired remanences, and being sufficiently molten to drive an active dynamo when Esquel acquired its remanence. We found that both inward and outward core growth are consistent with our X-PEEM results, and therefore both solidification styles are considered in the context of dynamo generation.

We present a simple model of dynamo generation via inner core nucleation where the onset of core solidification is accompanied by a rapid increase in magnetic field intensity (Figure 6). There is a gradual decrease in dynamo strength as the liquid, convecting outer shell reduces in volume throughout solidification. This mechanism of core solidification can sustain a long-lived dynamo, supported by current observations of Earth's magnetic field, and modeling of long-lived lunar dynamo activity (Laneuville et al., 2014). If the dynamo was only active for some fraction of the total core solidification time, then the maximum possible magnetic field intensities will be higher; however, our measured paleointensity for the Springwater pallasites ( $22 \pm 8 \mu\text{T}$ ), which corresponds to the maximum field strength shortly after the onset of a compositional dynamo, suggests that the mean intensity must be relatively weak ( $<20 \mu\text{T}$ ). This is consistent with the long lifetime of the dynamo ( $>117 \pm 4 \text{ Myr}$ ), which corresponds to the time between Springwater and Esquel acquiring remanence.

We found that a dynamo driven by inner core nucleation is difficult to reconcile with our upper paleointensity limits for Imilac and Esquel and the results reported by Tarduno et al. (2012). As the inner core crystallizes, the dynamo loses power, at odds with the apparent increase in paleointensity recorded by Springwater, Imilac, and Esquel, respectively. This discrepancy cannot be explained by the greater depth of each pallasite within the parent body (Table 4), which only accounts for a small increase in intensity. Additionally, the total energy in the core is insufficient to explain the paleointensities recorded by Imilac and Esquel at their modeled depths within the parent body, even for the shortest possible dynamo duration (Figure 7).

Given the small planetesimal sizes derived from our cooling models, the core is at low pressure, which suggests that core solidification is in fact more likely to be initiated at the core–mantle boundary (Hauck et al., 2006; Williams, 2009). We therefore also consider inward core solidification but do not attempt to

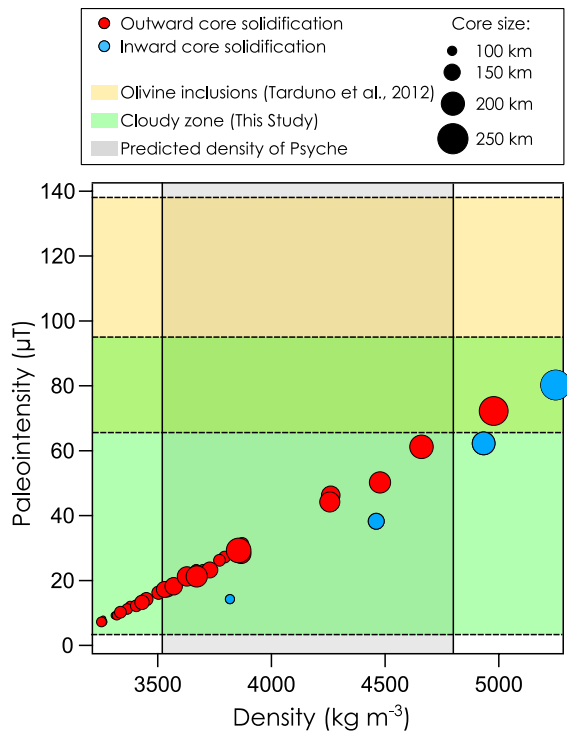


**Figure 8.** The magnetic field intensity versus planetesimal density predicted for each of our cooling models assuming an average density of  $7,000 \text{ kg m}^{-3}$  for the core and  $3,000 \text{ kg m}^{-3}$  for the mantle. Red points are for our thermal models for outward core solidification. Blue points are for our thermal models for inward core solidification. The size of the point represents the size of the planetesimal core. The yellow region represents the paleointensity results reported by Tarduno et al. (2012) for Imilac and Esquel. The green region represents the paleointensities reported here from X-PEEM studies of Springwater, Imilac, and Esquel. The yellow-green region shows where independent paleointensity estimates overlap. The gray region represents the predicted density of asteroid (16) Psyche (Drummond et al., 2018). X-PEEM, X-ray photoemission electron microscopy.

model the corresponding dynamo evolution since this is a relatively unexplored phenomena, particularly for a mantled planetesimal. However, model results have demonstrated that inward core solidification can drive a dynamo (Neufeld et al., 2019; Scheinberg et al., 2016) and that some asteroid cores solidified in such a manner (Yang et al., 2007). We find that both inward and outward core solidification of a planetesimal with a large core and thin mantle can explain both the timings of pallasite remanence acquisition relative to core solidification, and the high paleointensities and dynamo lifetime required by our recovered paleomagnetic record (Figure 7). We therefore conclude that a large core ( $>200 \text{ km}$  radius) and small mantle thickness ( $<70 \text{ km}$ ) are more important for generating high paleointensities than inward versus outward core solidification.

#### 4.4. Implications for the Origin of Pallasites

A recent study suggested that the pallasites may be the result of the propagation of metallic dykes from the core–mantle boundary into a shallow overlying mantle (Johnson et al., 2019). This study predicts that for high sulfur compositions ( $\sim 31 \text{ wt\%}$ ), metallic dykes could penetrate tens of kilometers into the mantle. This is consistent with our model results for inward core solidification (Table 4) which suggest that the pallasite parent body had a large metallic core with a high sulfur content and the pallasites could have originated from short distances ( $\sim 30 \text{ km}$ ) above the core–mantle boundary. This also demonstrates that the pallasites could form close to the core–mantle boundary while still originating in the mid-mantle of their parent planetesimal as suggested by previous studies (Bryson et al., 2015; Tarduno et al., 2012; Yang et al., 2010).

Pallasites have also been suggested to have formed throughout the parent body mantle, with the metal representing residual melt left over from incomplete differentiation (Boesenberg et al., 2012; Mckibbin et al., 2019). Textural and geochemical evidence suggests that in addition to residual metallic melt in the mantle, differentiated metal from an impactor must also play a role in pallasite formation in order to explain the range of observed textures (Tarduno et al., 2012; Walte et al., 2020). To reconcile these parent body configurations, where slow-cooled pallasites form close to the core–mantle boundary but also acquire a paleomagnetic record of a convecting, liquid core requires inward core solidification (Mck-

ibbin et al., 2019), consistent with our results. We also note however, that if the pallasite parent body only underwent partial differentiation, the metallic core will be relatively small, at odds with the energy required to drive a sustained, high-intensity dynamo (Figure 7). This may suggest that the parent body must be relatively large (radius  $>300 \text{ km}$ ) in order to partially differentiate and still form a core large enough to explain the observed paleointensities.

It has also been hypothesized that the pallasites may form within a planetesimal similar to the metallic asteroid (16) Psyche (Elkins-Tanton et al., 2020; Johnson et al., 2019; Walte et al., 2020). Current estimates suggest that Psyche has a density of  $4,160 \pm 640 \text{ kg m}^{-3}$  (Drummond et al., 2018). This is comparable to the density for many of our planetesimal models, assuming the core has a density of  $7,000 \text{ kg m}^{-3}$  and the mantle has a density of  $3,000 \text{ kg m}^{-3}$  (Figure 8). For our cooling models where intensities are consistent with our X-PEEM observations, the model planetesimals have a similar density to Psyche. To explain both our X-PEEM observations and the paleointensities recovered from olivine inclusions (Tarduno et al., 2012) require a large-cored and thinly mantled planetesimal with a density slightly higher than current predictions for Psyche.

## 5. Conclusions

We have presented new paleomagnetic data for the Springwater pallasite which “fills the gap” between Brenham and Marjalahti acquiring remanence prior to core solidification (Nichols et al., 2016), and Imilac and Esquel acquiring remanence after core solidification had begun and a compositional dynamo was active (Bryson et al., 2015; Tarduno et al., 2012). We have reassessed all X-PEEM data for the pallasites in light of advances in the technique and our understanding of remanence acquisition in the cloudy zone (Bryson et al., 2019; Einsle et al., 2018; Maurel et al., 2019). In addition, we conducted thermal and AF demagnetization experiments on olivines from the Springwater and Imilac pallasites. We found that AF techniques were not well suited for isolating directions or intensities in the samples analyzed. The extensive time (years) required to extract paleointensities from pallasite olivines, and issues with thermal alteration during controlled-atmosphere experiments, highlights the benefit of conducting paleomagnetic analyses on the cloudy zone rather than silicate inclusions in extraterrestrial samples with variable oxygen fugacities. However, previous paleointensity estimates from pallasite olivines (Tarduno et al., 2012) are critical for corroborating our cloudy zone paleointensities; the fact that both yield similar results indicating a past magnetization gives us confidence in our further consideration of the interior dynamics and structure of the pallasite parent body.

We present the most complete time-resolved paleomagnetic record for a planetesimal to date. Our results constrain the onset of core solidification and give a minimum time for core solidification, allowing the size and thermal evolution of the MG pallasite parent body to be well determined. We found that our X-PEEM results are consistent with both inward and outward core solidification, and the temporal trend in paleointensities is consistent with a dynamo driven by inner core solidification. However, to explain the upper limit on our paleointensity determinations for Imilac and Esquel and the strong paleointensities recovered by Tarduno et al. (2012), we show that a planetesimal with a large core and thin mantle is required. Strong paleointensities ( $\sim 65\text{--}95\ \mu\text{T}$ ) in the middle of a thin mantle can be generated by either inward or outward core crystallization. A dynamo driven by inward crystallization has been proposed for the asteroid (16) Psyche (Neufeld et al., 2019; Scheinberg et al., 2016). We show that the pallasites could form relatively close to the core–mantle boundary, while still forming in the middle of a thin mantle as predicted by previous studies (Bryson et al., 2015; Tarduno et al., 2012; Yang et al., 2010). We conclude that the pallasites could form on a planetesimal like asteroid (16) Psyche and could form by the intrusion of sulfur-rich metallic dykes through the mantle from the underlying core (Johnson et al., 2019).

Future studies should focus on directly determining the thermochronology of the pallasites. Our thermal models for outward versus inward core solidification provide contrasting predictions for the timing of remanence acquisition and the size of the parent body (Figure 7). Combined thermochronologic and paleomagnetic studies on suites of meteorites from the same parent body can provide a wealth of information regarding the size, internal structure, and dynamics of planetesimals.

## Data Availability Statement

All data associated with this study are available on Zenodo (<https://doi.org/10.5281/zenodo.4672000>) (Nichols et al., 2021).

## References

- Aubert, J., Labrosse, S., & Poitou, C. (2009). Modelling the palaeo-evolution of the geodynamo. *Geophysical Journal International*, 179(3), 1414–1428. <https://doi.org/10.1111/j.1365-246X.2009.04361.x>
- Boesenberg, J. S., Delaney, J. S., & Hewins, R. H. (2012). A petrological and chemical reexamination of Main Group pallasite formation. *Geochimica et Cosmochimica Acta*, 89, 134–158. <https://doi.org/10.1016/j.gca.2012.04.037>
- Brett, R., & Sato, M. (1984). Intrinsic oxygen fugacity measurements on seven chondrites, a pallasite, and a tektite and the redox state of meteorite parent bodies. *Geochimica et Cosmochimica Acta*, 48, 111–120.
- Bryson, J. F. J., Church, N. S., Kasama, T., & Harrison, R. J. (2014). Nanomagnetic intergrowths in FeNi meteoritic metal. The potential for time resolved records of planetesimal dynamo fields. *Earth and Planetary Science Letters*, 388, 237–248. <https://doi.org/10.1016/j.epsl.2013.12.004>
- Bryson, J. F. J., Neufeld, J. A., & Nimmo, F. (2019). Constraints on asteroid magnetic field evolution and the radii of meteorite parent bodies from thermal modeling. *Earth and Planetary Science Letters*, 521, 68–78. <https://doi.org/10.1016/j.epsl.2019.05.046>

## Acknowledgments

We thank Beck Strauss and an anonymous reviewer for their constructive comments which improved the quality of this manuscript. This work was supported by the European Research Council under the European Union's Seventh Framework Programme (FP/2007–2013)/ERC grant agreement numbers 320750 and 312284. We acknowledge the Helmholtz-Zentrum Berlin for the use of the synchrotron radiation beam time at beamline UE49 of BESSY II. We thank the Natural History Museum, London, the American Museum of Natural History, and the Harvard Museum of Natural History for loan of samples. CION thanks the Simons Foundation (award #556352), The Geological Society, the Mineralogical Society of Great Britain, the Mineral Physics Group of Great Britain, Jesus College Cambridge, and the Royal Astronomical Society for funding. BPW thanks the NASA Solar System Workings program and T.F. Peterson, Jr. for support. JH-A thanks the Spanish MCINN Project (DWARFS MAT2017-83468-R). Work at the University of Rochester was supported by NSF grant EAR1656348 and NASA grant 80NSSC19K0510.

- Bryson, J. F. J., Nichols, C. I. O., Herrero-Albillos, J., Kronast, F., Kasama, T., Alimadadi, H., et al. (2015). Long-lived magnetism from solidification-driven convection on the pallasite parent body. *Nature*, *517*(7535), 472–475. <https://doi.org/10.1038/nature14114>
- Bryson, J. F. J., Weiss, B. P., Getzin, B., Abrahams, J. N. H., Nimmo, F., & Scholl, A. (2019). Paleomagnetic evidence for a partially differentiated ordinary chondrite parent asteroid. *Journal of Geophysical Research: Planets*, *124*, 1880–1898. <https://doi.org/10.1029/2019JE005951>
- Bryson, J. F. J., Weiss, B. P., Harrison, R. J., Herrero-Albillos, J., & Kronast, F. (2017). Paleomagnetic evidence for dynamo activity driven by inward crystallisation of a metallic asteroid. *Earth and Planetary Science Letters*, *472*, 152–163. <https://doi.org/10.1016/j.epsl.2017.05.026>
- Christensen, U. R., & Aubert, J. (2006). Scaling properties of convection-driven dynamos in rotating spherical shells and application to planetary magnetic fields. *Geophysical Journal International*, *166*(1), 97–114. <https://doi.org/10.1111/j.1365-246X.2006.03009.x>
- Coe, R. S., Grommé, S., & Mankinen, E. A. (1978). Geomagnetic paleointensities from radiocarbon-dated lava flows on Hawaii and the question of the Pacific nondipole low. *Journal of Geophysical Research*, *83*(B4), 1740–1756. <https://doi.org/10.1029/JB083iB04p01740>
- Crozaz, G., Sibley, S. F., & Tasker, D. R. (1982). Uranium in the silicate inclusions of stony-iron and iron meteorites. *Geochimica et Cosmochimica Acta*, *46*(5), 749–754. [https://doi.org/10.1016/0016-7037\(82\)90026-6](https://doi.org/10.1016/0016-7037(82)90026-6)
- Dodds, K., Bryson, J. F. J., Neufeld, J. A., & Harrison, R. J. (2021). The thermal evolution of planetesimals during accretion and differentiation: Consequences for dynamo generation by thermally-driven convection. *Journal of Geophysical Research: Planets*, *126*, e2020JE006704. <https://doi.org/10.1029/2020JE006704>
- Drummond, J. D., Merline, W. J., Benoit, C., Conrad, A., Reddy, V., Peter, T., et al. (2018). The triaxial ellipsoid size, density, and rotational pole of asteroid (16) Psyche from Keck and Gemini AO observations 2004–2015. *Icarus*, *305*, 174–185. <https://doi.org/10.1016/j.icarus.2018.01.010>
- Dunlop, J. D., & Ozdemir, O. (1997). *Rock magnetism fundamentals and frontiers*. Cambridge: Cambridge University Press.
- Ehlers, E. G. (1972). *Interpretation of geological phase diagrams*. San Francisco, CA: W.H. Freeman.
- Einsle, J. F., Eggeman, A. S., Martineau, B. H., Saghi, Z., Collins, S. M., Roberts, B., et al. (2018). Nanomagnetic properties of the meteorite cloudy zone. *Proceedings of the National Academy of Sciences of the United States of America*, *115*(49), E11436–E11445. <https://doi.org/10.1073/pnas.1809378115>
- Elkins-Tanton, L. T., Asphaug, E., Bell, J. F., Bercovici, H., Bills, B., Binzel, R., et al. (2020). Observations, meteorites, and models: A preflight assessment of the composition and formation of (16) Psyche. *Journal of Geophysical Research: Planets*, *125*, e2019JE006296. <https://doi.org/10.1029/2019JE006296>
- Elkins-Tanton, L. T., Weiss, B. P., & Zuber, M. T. (2011). Chondrites as samples of differentiated planetesimals. *Earth and Planetary Science Letters*, *305*, 1–10. <https://doi.org/10.1016/j.epsl.2011.03.010>
- Evans, A. J., Tikoo, S. M., & Andrews-Hanna, J. C. (2018). The case against an early lunar dynamo powered by core convection. *Geophysical Research Letters*, *45*, 98–107. <https://doi.org/10.1002/2017GL075441>
- Fuller, M., & Cisowski, S. M. (1989). Lunar paleomagnetism. In *Geophysics. Encyclopedia of Earth Science*. Boston, MA: Springer. [https://doi.org/10.1007/0-387-30752-4\\_83](https://doi.org/10.1007/0-387-30752-4_83)
- Garrick-Bethell, I., Weiss, B. P., Shuster, D. L., & Buz, J. (2009). Early lunar magnetism. *Science*, *323*(5912), 356–359. <https://doi.org/10.1126/science.1166804>
- Gattacceca, J., & Rochette, P. (2004). Toward a robust normalized magnetic paleointensity method applied to meteorites. *Earth and Planetary Science Letters*, *227*(3–4), 377–393. <https://doi.org/10.1016/j.epsl.2004.09.013>
- Greenwood, R. C., Franchi, I. A., Jambon, A., Barrat, J. A., & Burbine, T. H. (2006). Oxygen isotope variation in stony-iron meteorites. *Science*, *313*(5794), 1763–1765. <https://doi.org/10.1126/science.1128865>
- Hanuš, J., Marchis, F., & Āurech, J. (2013). Sizes of main-belt asteroids by combining shape models and Keck adaptive optics observations. *Icarus*, *226*(1), 1045–1057. <https://doi.org/10.1016/j.icarus.2013.07.023>
- Hauck, S. A., Aurnou, J. M., & Dombard, A. J. (2006). Sulfur's impact on core evolution and magnetic field generation on Ganymede. *Journal of Geophysical Research*, *111*, E09008. <https://doi.org/10.1029/2005JE002557>
- Holmes, R. D. & Arculus, R. J. (1982). Metal-silicate redox reactions: Implications for core–mantle equilibrium and the oxidation state of the upper mantle. *Abstracts of Papers presented to the conference on planetary volatiles, held in Alexandria, MN, October 9–12, 1982*, *53*(9), 1689–1699. <https://doi.org/10.1017/CBO9781107415324.004>
- Johnson, B. C., Sori, M. M., & Evans, A. J. (2019). Ferrovolcanism on metal worlds and the origin of pallasites. *Nature Astronomy*, *4*, 41–44. <https://doi.org/10.1038/s41550-019-0885-x>
- Kronast, F., Schlichting, J., Radu, F., Mishra, S. K., Noll, T., & Dürr, H. A. (2010). Spin-resolved photoemission microscopy and magnetic imaging in applied magnetic fields. *Surface and Interface Analysis*, *42*(10–11), 1532–1536. <https://doi.org/10.1002/sia.3561>
- Laneuville, M., Wieczorek, M. A., Breuer, D., Aubert, J., Morard, G., & Rückriemen, T. (2014). A long-lived lunar dynamo powered by core crystallization. *Earth and Planetary Science Letters*, *401*, 251–260. <https://doi.org/10.1016/j.epsl.2014.05.057>
- Maurel, C., Weiss, B. P., & Bryson, J. F. J. (2019). Meteorite cloudy zone formation as a quantitative indicator of paleomagnetic field intensities and cooling rates on planetesimals. *Earth and Planetary Science Letters*, *513*, 166–175. <https://doi.org/10.1016/j.epsl.2019.02.027>
- Mckibbin, S. J., Pittarello, L., Makarona, C., Hamann, C., Hecht, L., Chernozhukhin, S. M., et al. (2019). Petrogenesis of main group pallasite meteorites based on relationships among texture, mineralogy, and geochemistry. *Meteoritics & Planetary Science*, *54*, 2814–2844. <https://doi.org/10.1111/maps.13392>
- Neufeld, J. A., Bryson, J. F. J., & Nimmo, F. (2019). The top-down solidification of iron asteroids driving dynamo evolution. *Journal of Geophysical Research: Planets*, *124*, 1331–1356. <https://doi.org/10.1029/2018JE005900>
- Nichols, C. I. O., Bryson, J. F. J., Cottrell, R. D., Fu, R. R., Harrison, R. J., Herrero-Albillos, J., et al. (2021). A time-resolved paleomagnetic record of the main group pallasites: Evidence for a Psyche-like parent body [Data set]. <https://doi.org/10.5281/ZENODO.4672000>
- Nichols, C. I. O., Bryson, J. F. J., Herrero-Albillos, J., Kronast, F., Nimmo, F., Richard, J., & Harrison (2016). Pallasite paleomagnetism: Quiescence of a core dynamo. *Earth and Planetary Science Letters*, *441*, 103–112.
- Nichols, C. I. O., Krakow, R., Herrero-Albillos, J., Kronast, F., Northwood-Smith, G., & Harrison, R. J. (2018). Microstructural and paleomagnetic insight into the cooling history of the IAB parent body. *Geochimica et Cosmochimica Acta*, *229*, 1–19. <https://doi.org/10.1016/j.gca.2018.03.009>
- Nimmo, F. (2009). Energetics of asteroid dynamos and the role of compositional convection. *Geophysical Research Letters*, *36*, L10201. <https://doi.org/10.1029/2009GL037997>
- O'Brien, T., Tarduno, J. A., Anand, A., Carroll-nellenback, J., Krot, A. N., V Smirnov, A., & Blackman, E. G. (2020). Arrival and magnetization of carbonaceous chondrites in the asteroid belt before 4562 million years ago. *Communications Earth & Environment*, *1*, 54. <https://doi.org/10.1038/s43247-020-00055-w>

- Righter, K., Arculus, R. J., Delano, J. W., & Paslick, C. (1990). Electrochemical measurements and thermodynamic calculations of redox equilibria in pallasite meteorites: Implications for the eucrite parent body. *Geochimica et Cosmochimica Acta*, 54(6), 1803–1815. [https://doi.org/10.1016/0016-7037\(90\)90409-E](https://doi.org/10.1016/0016-7037(90)90409-E)
- Scheinberg, A., Elkins-Tanton, L. T., Schubert, G., & Bercovici, D. (2016). Core solidification and dynamo evolution in a mantle-stripped planetesimal. *Journal of Geophysical Research: Planets*, 121, 2–20. <https://doi.org/10.1002/2015JE004843>
- Stephenson, A., & Collinson, D. W. (1974). Lunar magnetic field palaeointensities determined by an anhysteretic remanent magnetization method. *Earth and Planetary Science Letters*, 23, 220–228. [https://doi.org/10.1016/0012-821X\(74\)90196-4](https://doi.org/10.1016/0012-821X(74)90196-4)
- Suavet, C., Weiss, B. P., & Grove, T. L. (2014). Controlled-atmosphere thermal demagnetization and paleointensity analyses of extraterrestrial rocks. *Geochemistry, Geophysics, Geosystems*, 15, 2733–2743. <https://doi.org/10.1002/2013GC005215>
- Tarduno, J. A., & Cottrell, R. D. (2013). *Paleomagnetism of the Springwater Pallasite: Further evidence for a dynamo in the Main Group Pallasite Parent Body*. Paper presented at 44th Lunar and Planetary Science Conference, No. 2801.
- Tarduno, J. A., Cottrell, R. D., Nimmo, F., Hopkins, J., Voronov, J., Erickson, A., et al. (2012). Evidence for a dynamo in the main group pallasite parent body. *Science*, 338(6109), 939–942. <https://doi.org/10.1126/science.1223932>
- Tarduno, J. A., Cottrell, R. D., & Smirnov, A. V. (2006). The paleomagnetism of single silicate crystals: Recording geomagnetic field strength during mixed polarity intervals, superchrons, and inner core growth. *Reviews of Geophysics*, 44, RG1002. <https://doi.org/10.1029/2005RG000189>
- Tauxe, L., & Staudigel, H. (2004). Strength of the geomagnetic field in the Cretaceous Normal Superchron: New data from submarine basaltic glass of the Troodos Ophiolite. *Geochemistry, Geophysics, Geosystems*, 5, Q02H06. <https://doi.org/10.1029/2003GC000635>
- Tikoo, S. M., Weiss, B. P., Buz, J., Lima, E. A., Shea, E. K., Melo, G., et al. (2012). Magnetic fidelity of lunar samples and implications for an ancient core dynamo. *Earth and Planetary Science Letters*, 337, 93–338103. <https://doi.org/10.1016/j.epsl.2012.05.024>
- Tikoo, S. M., Weiss, B. P., Cassata, W. S., Shuster, D. L., Gattacceca, J., Lima, E. A., et al. (2014). Decline of the lunar core dynamo. *Earth and Planetary Science Letters*, 404, 89–97. <https://doi.org/10.1016/j.epsl.2014.07.010>
- Walte, N. P., Solferino, G. F. D., Golabek, G. J., Danielle Silva Souza, & Bouvier, A. (2020). Two-stage formation of pallasites and the evolution of their parent bodies revealed by deformation experiments. *Earth and Planetary Science Letters*, 546, 116419. <https://doi.org/10.1016/j.epsl.2020.116419>
- Wasson, J. T., & Choi, B.-G. (2003). Main-group pallasites: Chemical composition, relationship to IIIAB irons, and origin. *Geochimica et Cosmochimica Acta*, 67(16), 3079–3096. [https://doi.org/10.1016/S0016-7037\(03\)00306-5](https://doi.org/10.1016/S0016-7037(03)00306-5)
- Williams, Q. (2009). Bottom-up versus top-down solidification of the cores of small solar system bodies: Constraints on paradoxical cores. *Earth and Planetary Science Letters*, 284(3–4), 564–569. <https://doi.org/10.1016/j.epsl.2009.05.019>
- Yang, J., Goldstein, J. I., & Scott, E. R. D. (2007). Iron meteorite evidence for early formation and catastrophic disruption of protoplanets. *Nature*, 446(7138), 888–891. <https://doi.org/10.1038/nature05735>
- Yang, J., Goldstein, J. I., & Scott, E. R. D. (2010). Main-group pallasites: Thermal history, relationship to IIIAB irons, and origin. *Geochimica et Cosmochimica Acta*, 74(15), 4471–4492. <https://doi.org/10.1016/j.gca.2010.04.016>

## References From the Supporting Information

- Fu, R. R., Lima, E. A., Volk, M. W. R., & Trubko, R. (2020). High-sensitivity moment magnetometry with the quantum diamond microscope. *Geochemistry, Geophysics, Geosystems*, 21, e2020GC009147. <https://doi.org/10.1029/2020GC009147>
- Glenn, D. R., Fu, R. R., Kehayias, P., Sage, L. D., Lima, E. A., Weiss, B. P., & Walsworth, R. L. (2017). Micrometer-scale magnetic imaging of geological samples using a quantum diamond microscope. *Geochemistry, Geophysics, Geosystems*, 18, 3259–3267. <https://doi.org/10.1002/2017GC006946>
- Muxworthy, A. R., & Williams, W. (2015). Critical single-domain grain sizes in elongated iron particles: Implications for meteoritic and lunar magnetism. *Geophysical Journal International*, 202(1), 578–583. <https://doi.org/10.1093/gji/ggv180>

**A time-resolved paleomagnetic record of Main Group pallasites: Evidence for a large-cored, thin-mantled planetesimal**

Claire I.O. Nichols<sup>a,b</sup>, James F.J. Bryson<sup>b</sup>, Rory D. Cottrell<sup>c</sup>, Roger R. Fu<sup>d</sup>, Richard J. Harrison<sup>e</sup>, Julia Herrero-Albillos<sup>f,g</sup>, Florian Kronast<sup>h</sup>, John A. Tarduno<sup>c</sup>, Benjamin P. Weiss<sup>a</sup>

<sup>a</sup>Department of Earth, Atmospheric and Planetary Sciences, Massachusetts Institute of Technology, Cambridge, MA 02139, USA

<sup>b</sup>Department of Earth Sciences, University of Oxford, Oxford, OX1 3AN, UK

<sup>c</sup>Department of Earth and Environmental Sciences, University of Rochester, NY 14627, USA

<sup>d</sup>Department of Earth and Planetary Sciences, Harvard University, Cambridge MA, USA

<sup>e</sup>Department of Earth Sciences, University of Cambridge, Cambridge, CB2 3EQ, UK

<sup>f</sup>Centro Universitario de la Defensa, Carretera de Huesca s/n, E-50090 Zaragoza, Spain

<sup>g</sup>Instituto de Nanociencia y Materiales de Aragón (INMA), CSIC—Universidad de Zaragoza, Zaragoza 50009, Spain

<sup>h</sup>Helmholtz-Zentrum Berlin für Materialien und Energie, Albert-Einstein-Strasse 15, 12489 Berlin, Germany

## Contents of this file

Text S1 to S3

Figures S1 to S18

Tables S1 to S10

## Introduction

The following supplementary information contains additional experimental details for X-PEEM, SEM and superconducting rock magnetometer results reported in the paper. Additional details of the thermal and dynamo models are also included.

## Text S1.

### X-ray photoemission electron microscopy of the cloudy zone

#### S1.1 Beam intensity drift corrections

The X-ray beam intensity drifted slightly during measurements most likely due to minimal charging of the sample (Figure S1b). The intensity of images was corrected to account for this drift. A strict protocol was adopted for selecting images that can be corrected (Figure S1). The mean XMCD intensity was calculated for each set of 20 consecutive images taken with the same polarisation. Mean intensities were compared using a student's *T*-test, and were rejected if they were not statistically similar to 95% confidence. This inconsistency was attributed to light drift and only images whose mean intensities passed the *T*-test were used for further analysis.

XMCD images which passed the student's *T*-test were then used to calculate the six intensities representing the easy axis directions within the tetrataenite L<sub>1</sub><sub>0</sub> superstructure. A histogram of pixel intensity for the tetrataenite rim was calculated for each set of averaged images (Figure S2a & b). Since the six peaks represent three orthogonal axes, they should sit symmetrically about zero. It was found that for all three rotations, the average of equal and opposite peaks was slightly offset from zero due to beam instabilities (Figure S2c).

The offset,  $\Delta$ , was estimated by calculating the mean of the maximum XMCD intensities, shown in red  $R_i$  and blue  $B_i$  for each image, where the number of images is  $n$ .

$$\Delta = \frac{\sum_{i=1}^n (R_i + B_i)}{n}$$

As the sample is rotated relative to the X-ray beam, the average XMCD intensity varies; for a rotation of 180°, XMCD intensities of equal magnitude and opposite sign are recovered. Our corrected intensities vary as predicted for three rotations ~120° apart (Figure S3).

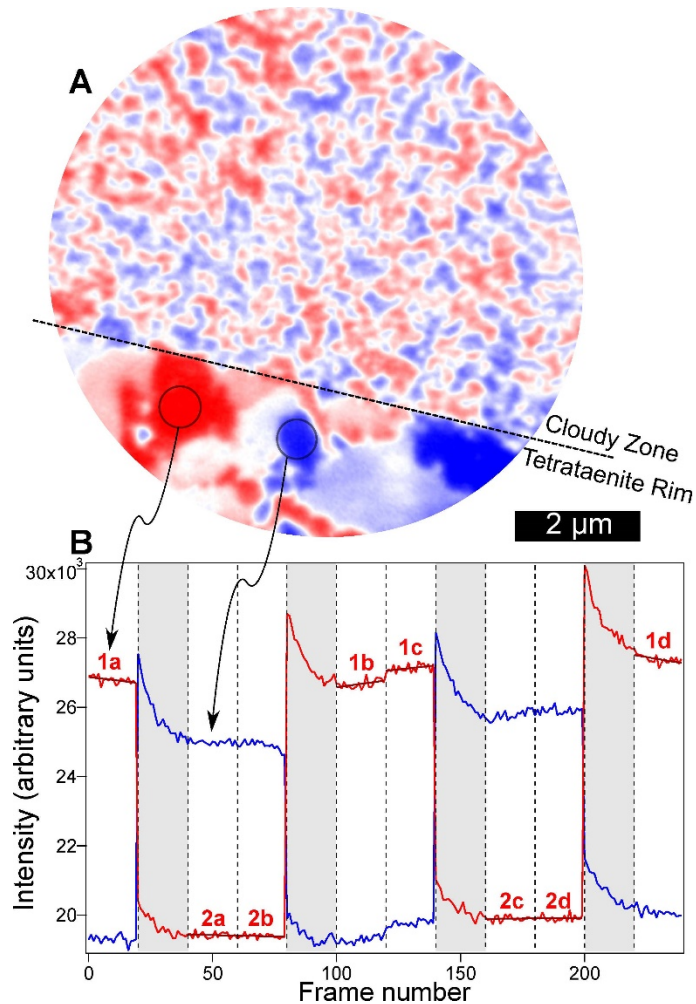


**Figure S1.** (a) XMCD image of the Springwater pallasite, showing a region of tetraetaenite rim and cloudy zone. This image is an average of 160 images each taken with a 2 second exposure time. Blue represents magnetisation away from the X-ray beam, red towards the X-ray beam and white perpendicular to the X-ray beam. The dashed line marks the boundary between the tetraetaenite rim and the cloudy zone. The two circles show regions selected for intensity drift assessment, taken from two adjacent domains with opposite magnetisation states. (b) Red and blue lines represent average intensity within the red and blue domains in the XMCD image shown in (a). The graph shows the variation in intensity for 240 consecutive images. Jumps at frame numbers 20, 80, 140 and 200 represent the change in polarisation of the X-ray beam. Immediately after each polarity change, a rapid decrease in intensity is observed; therefore the first 20 images after each polarity change are disregarded, allowing the intensity to settle (grey regions). A line of best fit is fitted to each block of 20 images, as shown here by red lines labelled 1a, 1b, 1c, 1d, 2a, 2b, 2c and 2d. A student's *T*-test was used to assess the similarity in intensity between 1a, b, c, d and 2a, b, c, d respectively. If the test failed the images were rejected, since drift of the X-ray beam during the measurements was too significant and has caused a bias in measurements that cannot be removed.

Rotation No.	Drift Correction
1	0.039
2	0.014
3	0.012

**Table S1.** Calculated correction offsets using tetraenaite rim intensities from the Springwater pallasite.

Rotation 1	Uncorrected CZ XMCD Intensity	Corrected CZ XMCD Intensity	Rotation 2	Uncorrected CZ XMCD Intensity	Corrected CZ XMCD Intensity	Rotation 3	Uncorrected CZ XMCD Intensity	Corrected CZ XMCD Intensity
X_0340	-0.020	0.019	X_0573	-0.007	0.007	X_0758	-0.027	-0.015
X_0384	-0.011	0.028	X_0598	-0.020	-0.006	X_0788	-0.033	-0.021
X_0399	0.001	0.040	X_0613	-0.016	-0.002	X_0813	-0.003	0.009
X_0429	0.002	0.041	X_0673	-0.023	-0.009	X_0833	-0.016	-0.004
X_0434	-0.009	0.030	X_0683	-0.017	-0.003	X_0871	-0.038	-0.026
X_0454	-0.001	0.038	X_0703	-0.013	0.001	X_0921	-0.019	-0.007
X_0464	0.004	0.043	X_0723	-0.007	0.007	X_0941	-0.022	-0.010
X_0479	0.013	0.052	X_0738	-0.017	-0.003	X_0967	-0.018	-0.006

**Table S2.** The analysed X-PEEM images of Springwater for each rotation, the average cloudy zone XMCD intensity for each region and the corrected intensities.

Rotation	$I_{-x}$	$I_x$	$I_{-y}$	$I_y$	$I_{-z}$	$I_z$
1	$-0.15 \pm 0.02$	$0.12 \pm 0.01$	$-0.08 \pm 0.02$	$0.08 \pm 0.02$	$-0.05 \pm 0.01$	$0.04 \pm 0.02$
2	$-0.06 \pm 0.01$	$0.05 \pm 0.02$	$-0.02 \pm 0.01$	$0.02 \pm 0.01$	$-0.13 \pm 0.03$	$0.12 \pm 0.03$
3	$-0.07 \pm 0.01$	$0.06 \pm 0.01$	$-0.14 \pm 0.02$	$0.14 \pm 0.02$	$-0.11 \pm 0.02$	$0.11 \pm 0.01$

**Table S3.** The tetraenaite rim intensities corresponding to the three orthogonal tetraenaite easy axis directions measured and averaged across X-PEEM images of Springwater for each rotation.

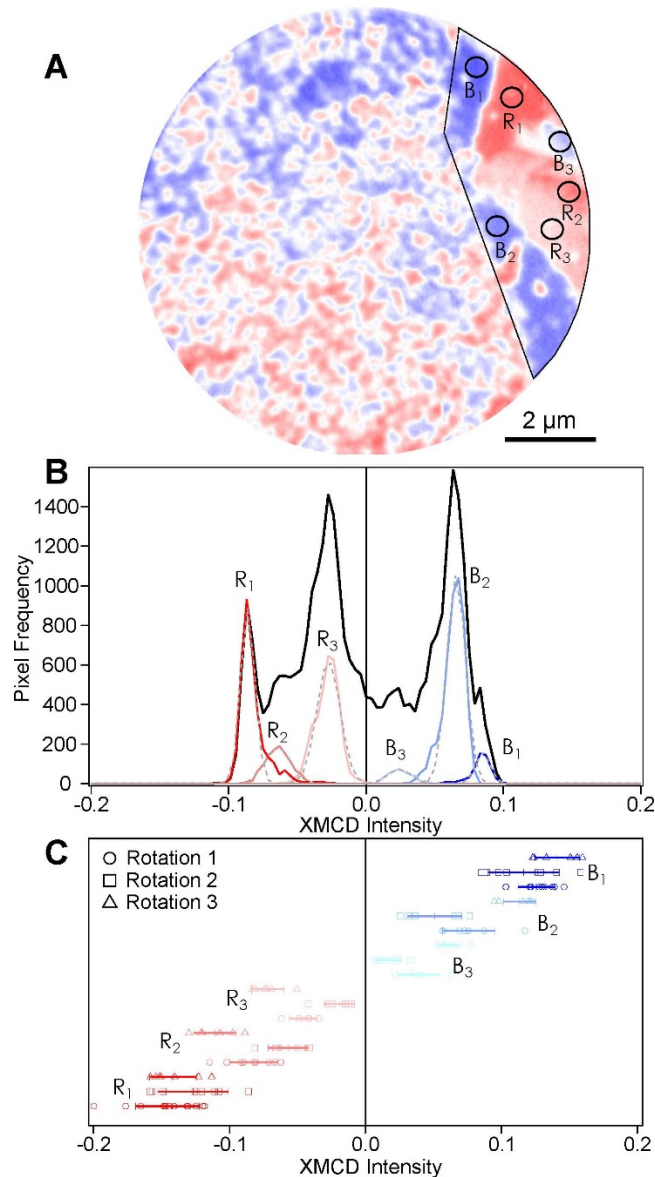


**Figure S2.** A histogram of pixel intensity is taken for the entire tetraenaite rim in each XMCD image of the Springwater pallasite, shown by the enclosed black line in (a) and the histogram defined by the black line in (b). Six distinct peaks contributing to this histogram were identified, representing the six easy axis directions in the ordered tetraenaite  $L_{10}$  superstructure. These are found by selecting regions with clear, distinct intensities, such as those shown by the grey circles labelled  $R_1 - R_3$  and  $B_1 - B_3$  in (a). Each region corresponds to the peaks labelled  $R_1 - R_3$  and  $B_1 - B_3$  in (b), with colours corresponding to their relative intensities. A Gaussian curve is then fitted to each of the six peaks, represented by the grey dashed curves. The peak and two standard deviations are recorded for each of the six curves. (c) The peak position of the six peaks,  $R_1$ ,  $R_2$ ,  $R_3$ ,  $B_1$ ,  $B_2$  and  $B_3$  are plotted for each rotation. Circles, square and triangles represent rotations 1, 2 and 3 respectively. The mean and two standard deviations are shown as a horizontal line for each set of peaks. The peaks for each rotation do not sit symmetrically about zero and therefore need to be corrected.

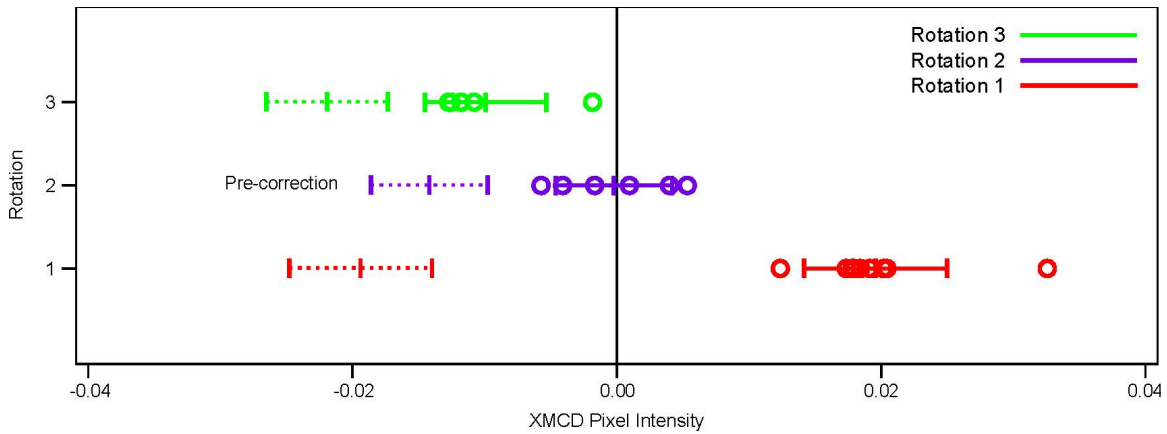


**Figure S3.** Open circles represent corrected histogram averages for the Springwater cloudy zone using Equation S1 for each averaged XMCD image of the cloudy zone. Red, purple and green represent rotations 1, 2 and 3 respectively. The average and two standard deviations in peak position are displayed for each rotation. All averages are very close to zero. However rotation 1 shows a slight positive offset and rotation 3 a slight negative offset, as predicted by the fact the relative change in magnetisation direction as the sample is rotated relative to the X-ray beam. The dotted lines show the position of the XMCD averages before correction, which are all negative.

### S1.2 Calculating uncertainty on one rotation X-PEEM paleointensity estimated

There is an inherent uncertainty in the paleointensities recovered for the Brenham, Marajalahti, Imilac and Esquel pallasites using X-PEEM since they were only imaged in one direction. We therefore know that we have recovered some component,  $I_{rec}$ , of the true NRM magnetization vector,  $I_{NRM}$ , which was parallel to the X-ray beam during our measurement. However, we do not know how the magnetization vector is aligned relative to the X-ray beam ( $\theta$ ), and therefore we only have limited constraints on the magnitude of  $I_{NRM}$ . We know the minimum strength is given by  $I_{NRM} = I_{rec}$  where  $\theta = 0^\circ$  and we know that  $I_{rec} = I_{NRM} \sin \theta$  (Figure S4a). To quantify the uncertainty on our estimate of  $I_{NRM}$ , we consider the probability we have measured the magnetization vector at any given angle of  $\theta$ . The probability of measuring any value of  $\theta$  is given by  $\cos \theta$ , which shows that high values of  $\theta$  are sampled more frequently than low values of  $\theta$  (Figure S4b). In other words, there is only one measurement configuration in which the X-ray beam is parallel to the remanence vector  $\theta = 0^\circ$ , while there are an increasing number of plausible configurations as the measurement angle  $\theta \rightarrow 90^\circ$ . To representatively sample  $\theta$ , we randomly sampled the cumulative distribution function  $\int \cos \theta d\theta$  (Figure S4c). We sampled 1000 values of  $\theta$  and then interpolated these to the corresponding values of  $I_{NRM}$  (Figure S4d). These bootstrapped values of  $I_{NRM}$  define a one-tailed distribution increasing from a minimum value of  $I_{rec}$  (Figure S4e). The cumulative density function for this one-tailed distribution was calculated by taking the cumulative integral of the one-tailed distribution (Figure S4f). We calculate the 95% confidence by taking the value of  $I_{NRM}$  that encompasses 95% of our bootstrapped intensity estimates. This process is repeated 100 times for any given value of  $I_{rec}$  and the mean value of the 95% confidence interval on  $I_{NRM}$  is reported (main text Table 3).

Region	Intensity ( $\mu$ T)	Trend / Plunge ( $^\circ$ )
1	14.9	076/-32
2	20.2	093/-34
3	23.2	089/16
4	22.9	094/-03
5	22.7	090/-39
6	21.7	086/-08
7	24.5	082/-12
8	28.2	090/-05
<b>Average</b>	<b>22 <math>\pm</math> 8</b>	<b>088/-15 <math>\alpha_{95}=14</math></b>

**Table S4.** The strength and relative direction of the paleomagnetic field recorded by eight regions of cloudy zone in Springwater, each imaged in three rotations.

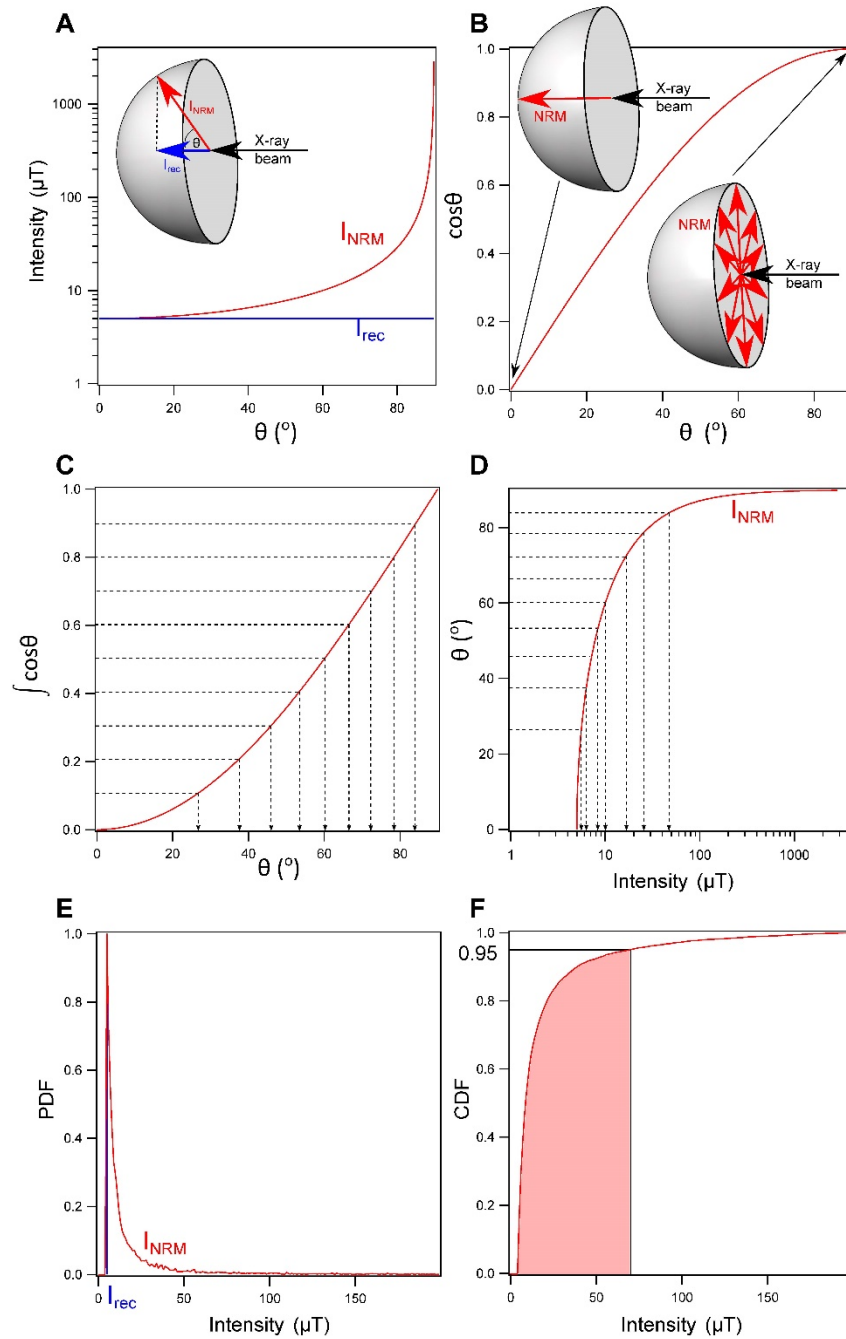


**Figure S4.** Schematic diagrams showing the bootstrapping approach for calculating the 95% confidence interval on X-PEEM paleointensities estimated from one rotation. **(a)** The magnitude of  $I_{NRM}$  as a function of  $I_{rec}$  and  $\theta$ . **(b)** The probably density function of  $\theta$  on a sphere is given by  $\cos \theta$ . **(c)** Possible measurement angles are representatively sampled by taking a random distribution of the cumulative distribution function  $\int \cos \theta$  and interpolating the corresponding values of  $\theta$ . **(d)** The representative sample of  $\theta$  values are used to calculate the corresponding values of  $I_{NRM}$ . **(e)** The probability density of bootstrapped values of  $I_{NRM}$  show a one-tailed distribution with a minimum value of  $I_{rec}$ . **(f)** The 95% confidence interval on  $I_{NRM}$  is calculated from the cumulative distribution function, such that 95% of the bootstrapped values of  $I_{NRM}$  are included.

## Text S2.

### Paleomagnetism and rock magnetism of pallasite olivines

#### S2.1 Sample preparation

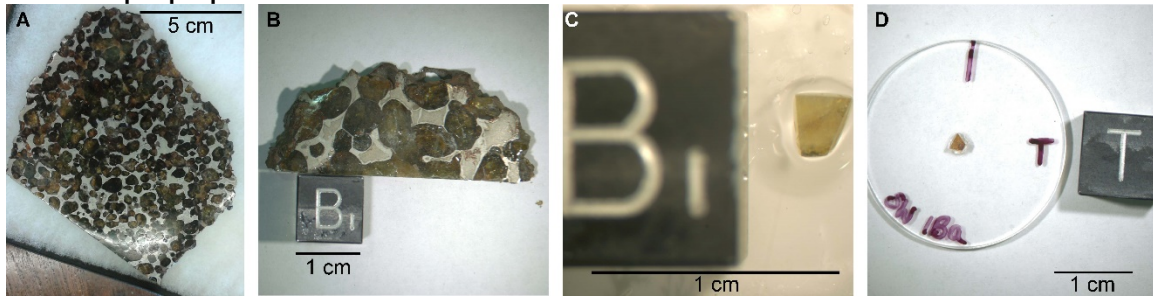


**Figure S5.** Sample preparation in the MIT Paleomagnetism Laboratory. **(a)** The sample of Springwater borrowed from the Harvard Museum of Natural History. **(b)** A small section of the slab was removed from the main slab of Springwater using a Buehler IsoMet low speed saw. **(c)** Small olivine subsamples were extracted using a Well precision diamond wire saw. An orientation cube is used to maintain orientation of samples before and after cutting. **(d)** Samples are mounted on quartz discs using either glue or tape.

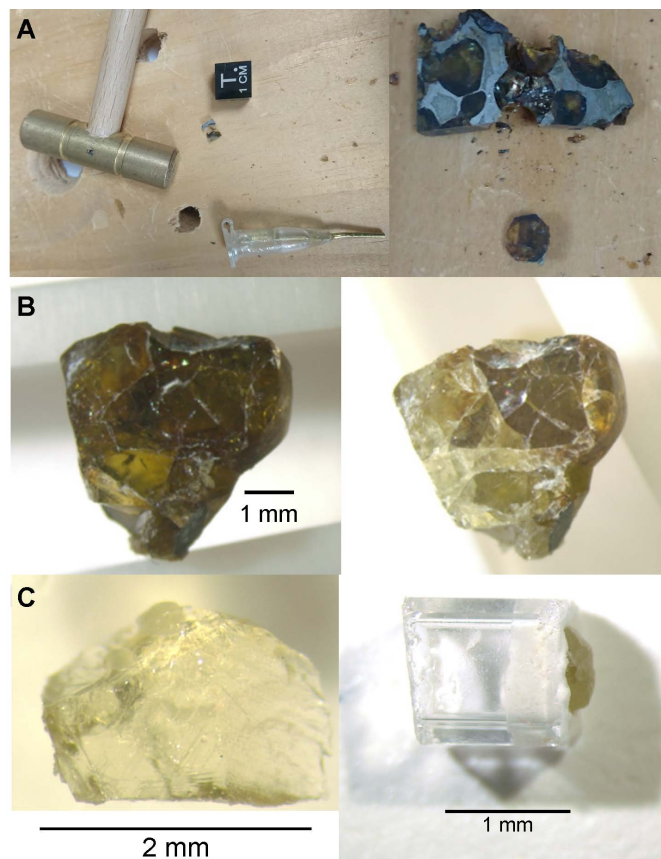


**Figure S6.** Sample preparation in the University of Rochester Paleomagnetism and Rock Magnetism Laboratory. **(a)** Olivines were extracted using a small copper hammer and chisel. Tapping on the boundary between an olivine and the FeNi metal causes olivines to 'pop' out of the matrix. **(b)** Samples were acid washed in 1 molar HCl acid for ~12 hours to remove oxides and altered olivine. Olivines look notably lighter after acid washing. **(c)** Gem quality samples are mounted in 1 mm<sup>3</sup> quartz boxes for measurement.

## S2.2 Alternating Field Experiments

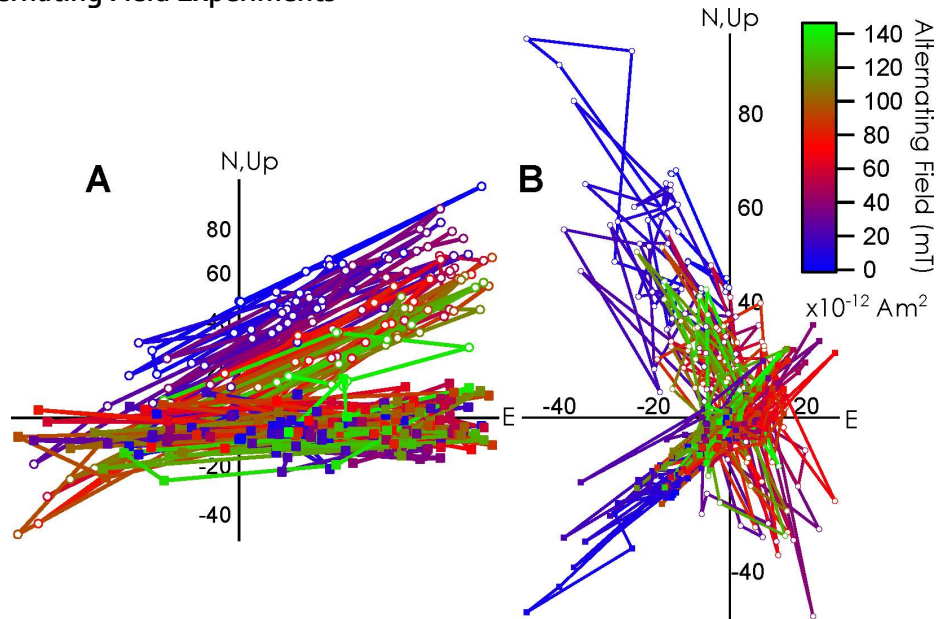


**Figure S7.** Zijdeveld plots for demagnetisation of a 100  $\mu\text{T}$  ARM for Springwater (a) SWH1Ea (b) SWH3Ba. Closed squares show declination, open circles show inclination, the colour bar represents the strength of AF demagnetization. There is one very clear axis defined throughout the entire coercivity spectrum for all samples. This is characterised by the antipodal flipping of pinned magnetisation vectors throughout demagnetisation.

Sample	Coercivity	L ( $\mu\text{T}$ )	I ( $\mu\text{T}$ )	W ( $\mu\text{T}$ )	D (%)	E (%)	Type
SW1Aa	HC	74.6	62.1	48.4	-16.8	64.9	100 $\mu\text{T}$ ARM vs IRM
	LC	74.6	200.7	51.6	169.0	69.2	
	HC	223.9	331.1	43.3	47.9	19.3	300 $\mu\text{T}$ ARM vs IRM
	LC	223.9	340.2	41.3	51.9	18.4	
	HC	74.6	41.1	29.5	-44.9	39.5	100 $\mu\text{T}$ ARM vs 300 $\mu\text{T}$ ARM
	LC	74.6	131	29.4	75.6	39.4	
SW1Ab	HC	74.6	-4.9	57.4	-106.6	76.9	100 $\mu\text{T}$ ARM vs IRM
	LC	74.6	137.6	35.7	84.5	47.9	
	HC	223.9	56.7	58.3	-74.7	26.0	300 $\mu\text{T}$ ARM vs IRM
	LC	223.9	391.2	67	74.7	29.9	
	HC	74.6	43.5	75.4	-41.7	101.1	100 $\mu\text{T}$ ARM vs 300 $\mu\text{T}$ ARM
	LC	74.6	79.1	13.6	6.0	18.2	
SWH1frag	HC	37.3	102.3	24.7	174.3	66.2	50 $\mu\text{T}$ ARM vs IRM
	LC	37.3	35.4	9.9	-5.1	26.5	
	HC	74.6	19.6	12.9	-73.7	17.3	100 $\mu\text{T}$ ARM vs IRM
	LC	74.6	3.2	11.2	-95.7	15.0	
	HC	37.3	137.6	88.8	268.9	238.1	50 $\mu\text{T}$ ARM vs 100 $\mu\text{T}$ ARM
	LC	37.3	10.8	33.8	-71.0	90.6	

**Table S5.** Statistical treatment of paleointensity estimates to assess their fidelity.  $L$  is the applied laboratory field.  $I$  is the retrieved paleointensity.  $W$  is the 95% confidence interval on the retrieved paleointensity.  $D$  is the percentage difference between the applied laboratory field and recovered paleointensity.  $E$  is the percentage error on the retrieved paleointensity compared to the magnitude of the applied laboratory field. *Type* refers to whether the paleointensity estimate was calculated from ARM lost vs ARM lost, or ARM lost vs IRM lost.

Sample	Mass (mg)	Type	Range (mT)	N	Dec (°)	Inc (°)	MAD (°)	dANG (°)	Origin trending?	Forced?
IM1Ba	0.045	LC	NRM - 7	14	140.4	2	23.5	73.8	No	No
		HC	7-17.5	22	151.7	4.6	33	61.6	No	Yes
IM1Bb	0.05154	LC	NRM - 7	14	72.3	-55	22.7	11.2	Yes	No
		HC	7 - 16.5	20	72.6	-30.6	29.3	8.9	Yes	Yes
IM1Be	0.00675	LC	NRM - 3.5	7	254.2	-8.6	16.4	58.2	No	No
		HC	3.5 - 78	97	251.3	-3.5	25.9	85.5	No	Yes
SW1Aa	-	LC	NRM - 13.5	27	9.1	-18.6	10.1	38.5	No	No
		HC	13.5 - 52	51	61.7	-13.2	17.7	22.2	No	Yes
SW1Ab	-	LC	NRM - 3.5	7	6.3	-46.6	4.2	35.4	No	No
		HC	3.5-18.5	31	23	8.5	13	18.2	No	Yes
SWH1Dd	0.02475	LC	0 - 5	10	328.5	4.8	35.3	18.9	Yes	No
		HC	5 - 13.5	18	344.1	60.2	34	8.6	Yes	Yes
SWH1Ea	0.0138	LC	0 - 2.5	5	1	62.4	0.5	45.7	No	No
		HC	2.5 - 3.5	3	349	57.9	20.5	7.7	Yes	Yes
SWH2Ad	0.01066	LC	0 - 5	10	311.6	-9.7	21.3	84.8	No	No
		HC	5 - 10	11	220	-56.7	8.1	0.1	Yes	Yes
SWH2Ba	0.012	LC	0 - 6	12	300.2	18.4	20.5	65.3	No	No
		HC	6 - 26	40	96.5	-11.7	26.9	5	Yes	Yes
SWH1frag	0.01261	LC	0 - 19	38	144.4	1.9	6.2	4.4	Yes	No
		HC	19 - 35	23	16.5	-17.3	4.35	1	Yes	Yes
SWH1Da	0.0194	LC	0 - 145	150	68.9	-47.6	13.5	51.2	No	No
		HC								Yes
SWH3Ba	-	LC	0 - 6	12	313.6	48.4	8.1	24.6	No	No
		HC	6 - 7.5	4	129.5	-61.3	22.7	4	Yes	Yes

**Table S6.** High and low coercivity components are calculated for each of the AF demagnetised samples. Columns one and two describe the subsample and its mass, respectively. Column three defines whether the fit is for the low or high coercivity component. Column four gives the coercivity range of the component and column five is the number of points within the component. Columns six, seven, eight and nine describe the declination, inclination, *MAD* and *dAng* of the fitted component, respectively. Column ten states whether the component is origin-trending, dictated by  $dAng < MAD$ . Column eleven states whether the component fit was forced through the origin.

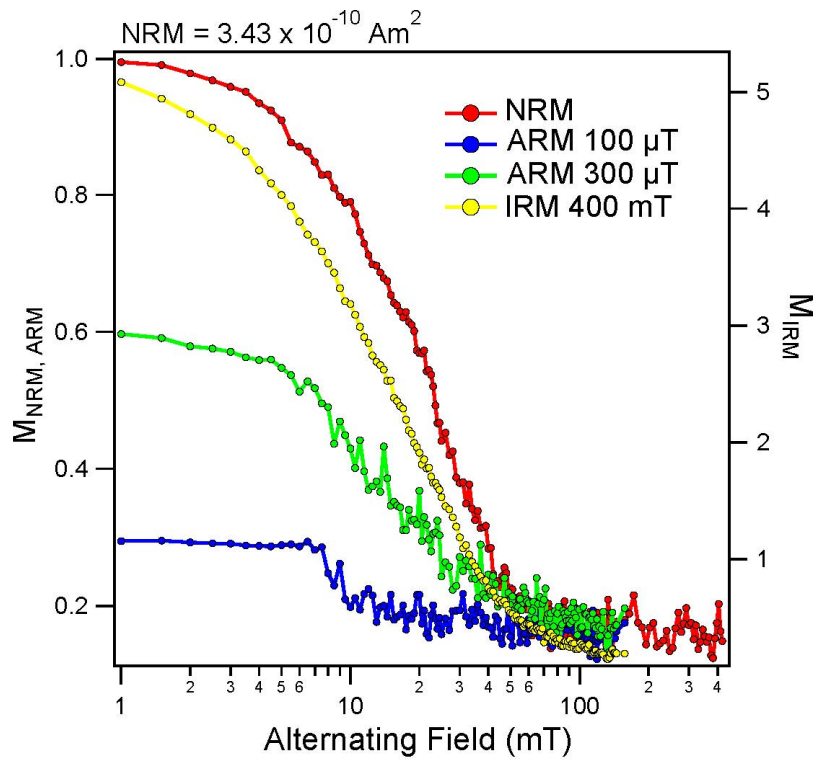


**Figure S8.** An example of the Springwater pallasite from the AMNH which has been exposed to a collector's hand magnet. NRM, ARM and IRM curves are normalized to the peak NRM value of  $3.43 \times 10^{-10} \text{ Am}^2$ . The shape of the NRM demagnetisation curve looks most similar to the 400-mT IRM demagnetisation curve, and has a much stronger moment than both a 100  $\mu\text{T}$  and 300  $\mu\text{T}$  ARM, implying it has experienced a stronger field than can be generated by a planetary dynamo.

Sample	Coercivity	Paleointensity ( $\mu\text{T}$ )		Type
		Mean	$2\sigma$	
SW1Aa	HC	105.5	69.6	NRM vs ARM
	LC	137.9	30.4	
	HC	353.2	50.2	NRM vs ARM
	LC	308.7	28.8	
	HC	621.4	45.8	NRM vs IRM
	LC	488	49.2	
SW1Ab	HC	26.3	94.3	NRM vs ARM
	LC	337.8	115.9	
	HC	301.3	238.6	NRM vs ARM
	LC	378.7	85.2	
	HC	487.8	75.7	NRM vs IRM
	LC	652.1	214.2	
SWH1Dd	HC	-24.4	28	NRM vs ARM
	LC	19.7	27.3	
SWH1Ea	HC	-102.7	151.5	NRM vs ARM
	LC	-1.1	22	
SWH2Ad	HC	12.7	82.7	NRM vs ARM
	LC	15.9	11.7	
SWH2Ba	HC	-4.9	64.1	NRM vs ARM
	LC	24.4	13.3	
SWH1frag	HC	14.7	10.4	NRM vs ARM
	LC	25.7	9.3	
	HC	52.3	77.1	NRM vs ARM
	LC	18.4	34	
	HC	68.6	23.9	NRM vs IRM
	LC	40	8.2	
SWH3Ba	HC	-18.1	102	NRM vs ARM
	LC	10.1	41.1	

**Table S7.** NRM paleointensity estimates calculated by comparing the AF demagnetisation of an NRM to either an ARM or a IRM. Paleointensity estimates were calculated for both low coercivity (LC) and high coercivity (HC) components. The mean and two standard deviations are given for each paleointensity estimate. It is also stated whether the estimate was calculated by comparing the NRM to an ARM or an IRM.

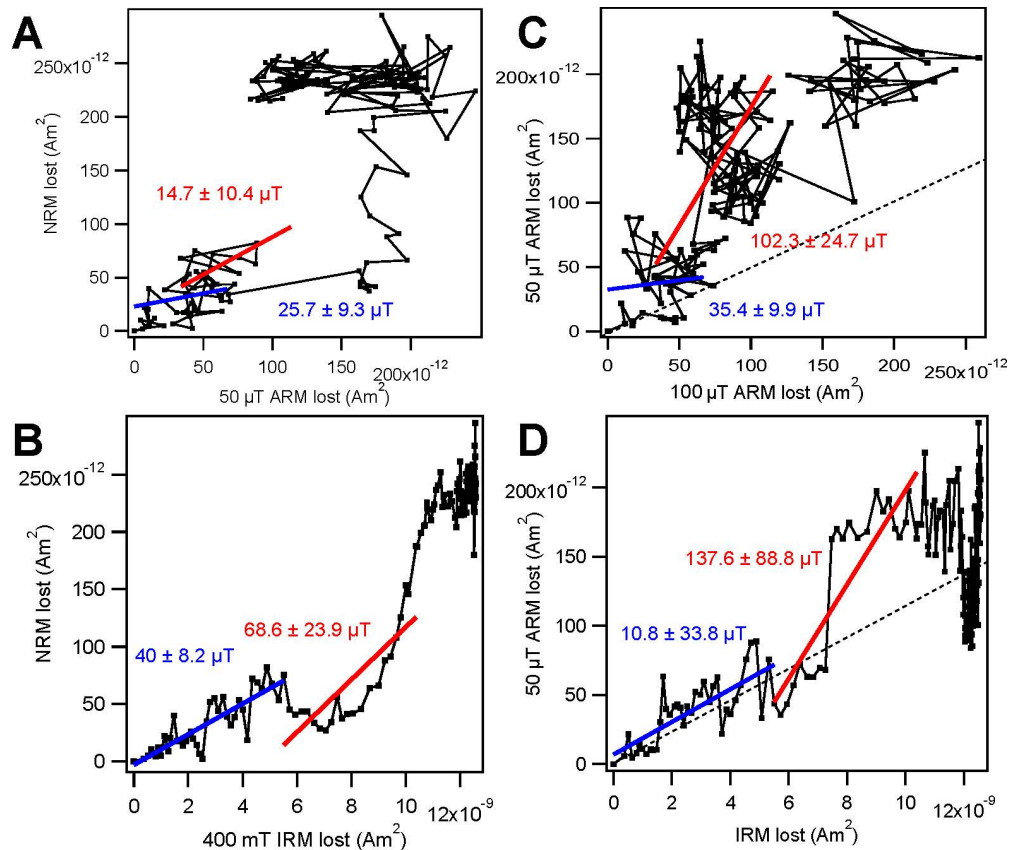


**Figure S9.** Examples of the plots used for paleointensity calculations (**a,b**) and fidelity tests (**c,d**). Examples are shown for a sample of Springwater, SWH1frag. The blue and red lines represent the low and high coercivity fits, respectively. These fits are used to estimate paleointensities. (**a**) Shows NRM lost versus a 50  $\mu\text{T}$  lost, where 'lost' refers to the moment removed by subsequent AF demagnetisation. (**b**) NRM lost is plotted against IRM lost. In (**c**) and (**d**) 50  $\mu\text{T}$  ARM lost is plotted against a stronger 100  $\mu\text{T}$  ARM lost and 400 mT IRM lost, respectively. In both cases, these plots should return paleointensity estimates corresponding to a TRM of  $\sim 37 \mu\text{T}$ , which is equivalent to a 50  $\mu\text{T}$  ARM. The dashed lines show the expected slope. This is therefore a good test of the fidelity of the paleomagnetic recorder.

### S2.3 Scanning Electron Microscopy

Silicate inclusions were imaged using the field emission gun scanning electron microscope (FEG-SEM) in the Department of Earth Sciences, University of Cambridge. Back scatter electron (BSE) and energy dispersive spectroscopy (EDS) data were collected in high vacuum mode using a dwell time of 5 – 25  $\mu\text{s}$ , an accelerating voltage between 5 and 15 kV and a working distance of 13.8 – 14 mm. Results were analysed using Bruker software.

BSE images of olivine inclusions were acquired, and their compositions semi-quantified using EDS. Acicular iron chromium oxide inclusions and strings of iron sulphide inclusions were observed. Quantified compositions of iron chromium oxide needles show they have a Cr:Fe ratio of 3.1 - 5.5:1. FeNi phases were found in association with FeS phases; for example, a cubic FeNi particle with a diameter of  $\sim 500$  nm is observed growing over an acicular FeS inclusion (Figure S10). The size of this FeNi inclusion suggests it is magnetically either single vortex or single domain (Muxworthy and Williams, 2015).

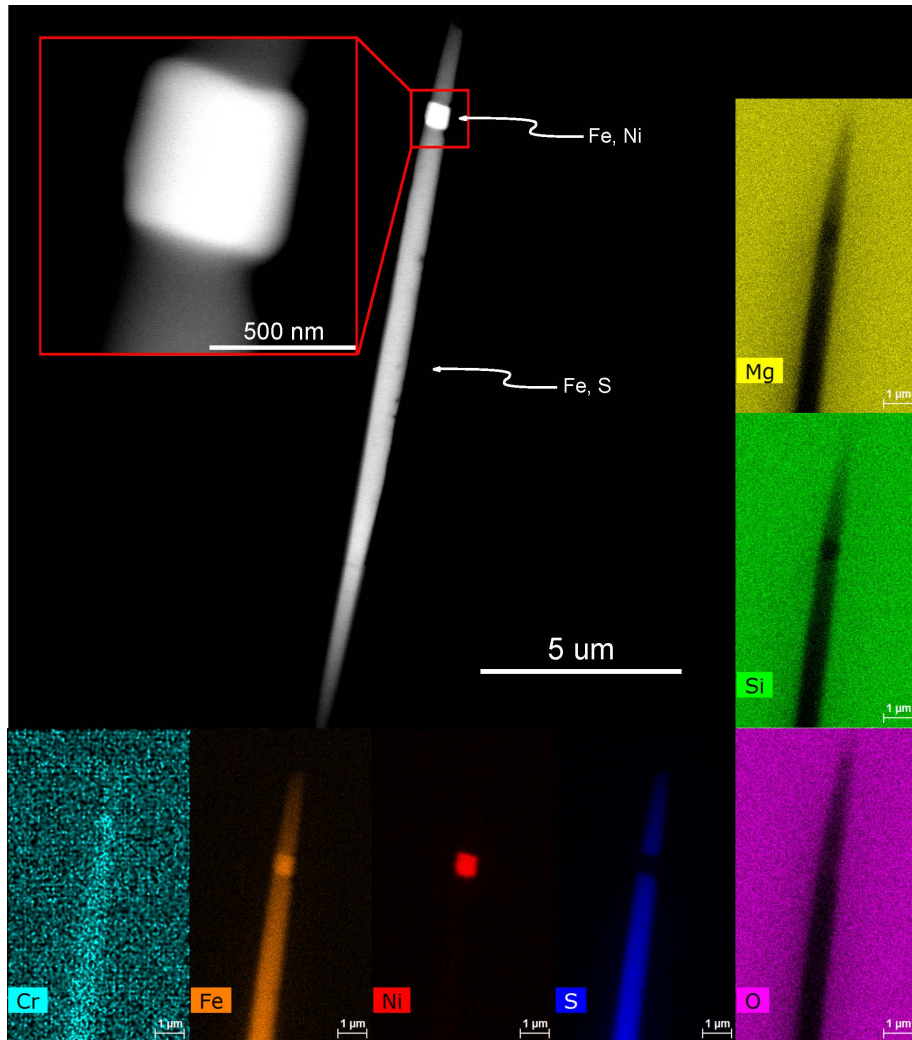


**Figure S10.** An inclusion in sample SWH2Ba of the Springwater pallasite. EDS data shows that the needle is FeS, and the small inclusion at the upper end of the needle is a small FeNi particle.

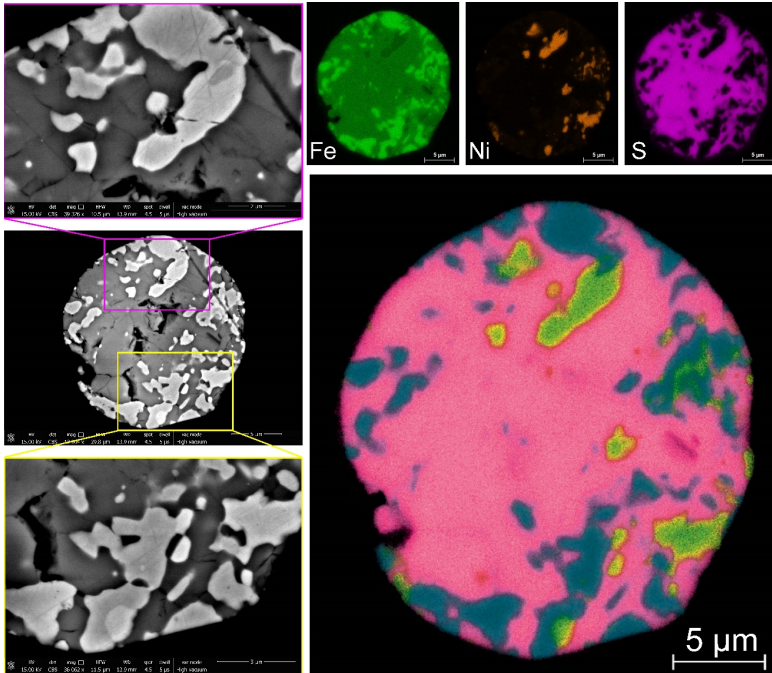


**Figure S11.** A troilite-FeNi metal intergrowth inclusion in sample IM1Be of the Imilac pallasite. BSE images show the difference between the darker Fe and S regions compared to the brighter Fe and Ni regions. There is further compositional variation within the bright regions; the brightest edges are the most Ni rich. We also show EDS maps for S, Fe and Ni, which are combined in the large image where pink is S, blue is Fe and yellow is Ni.

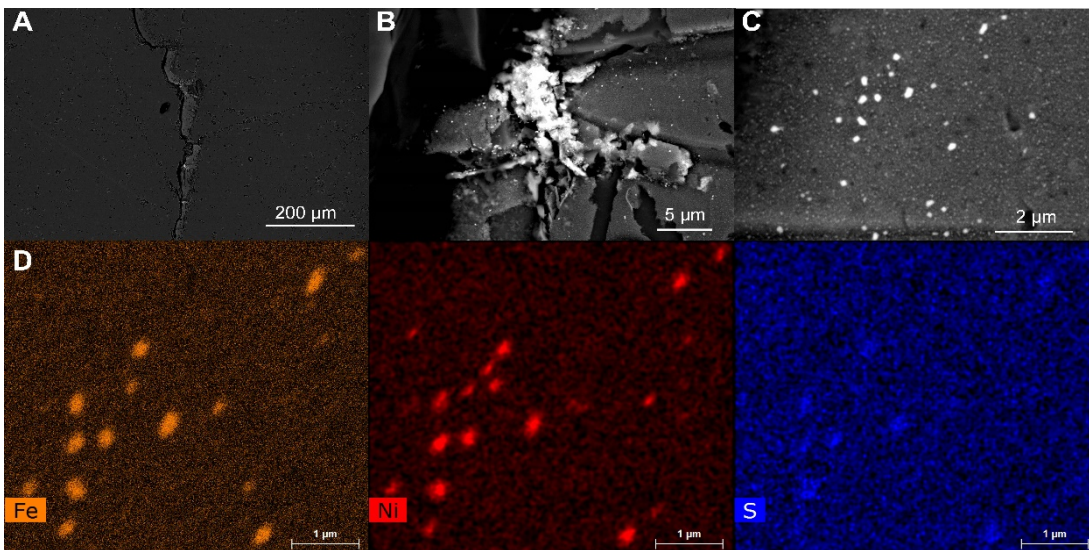


**Figure S12.** BSE images of IM3Ba from the Imilac pallasite which was heated to 500 °C. (a) Some cracks appear brighter than the surrounding olivine. The red box shows the region imaged in (b). (b) Cracks are characterised by abundant small inclusions with an FeNi composition. (c) Zoom in of some of the FeNi particles. (d) Fe map of the particles. (e) Ni map of the particles. (f) S map of the particles.

## S2.4 IRM Acquisition

IRM acquisition curves are used to ascertain the coercivity spectra for magnetic carriers trapped within Springwater olivines (Figure S13a). Three samples were measured, all of which show two clear peaks. The low coercivity component ranges from ~10 – 30 mT and the high coercivity component from ~60 – 70 mT. The low coercivity carrier is likely to be multidomain kamacite or taenite, and the higher coercivity component is consistent with single-domain or single-vortex FeNi grains as observed in Figure S10.

After applying a 100  $\mu\text{T}$  ARM and subsequently AF demagnetizing samples, some (such as SWH1Ea and SWH3Ba) showed significant pinning of the direction of magnetic moments (Figure S7). The magnetic moment flips between two antipodal directions, suggesting magnetic carriers have a high degree of anisotropy (Tikoo et al., 2012).

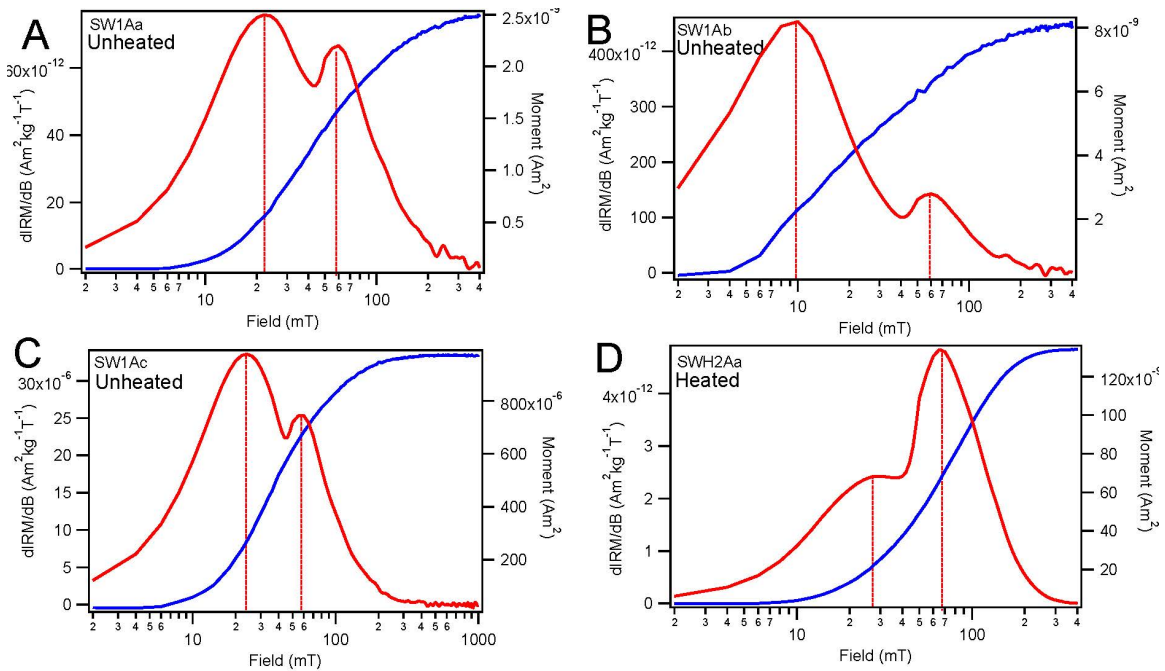


**Figure S13.** IRM acquisition curves are shown in blue for each sample and magnetic moment is given on the right hand axis. The differential of the IRM acquisition curves is shown in red and plotted on the left hand axis. In all cases two distinct coercivity populations are observed, most likely representing multidomain kamacite and single domain FeNi particles. For samples (a) SW1Aa, (b) SW1Ab and (c) SW1Ac, which are unheated, the bulk of the coercivity is in the range of 10 – 30 mT, with a higher coercivity range at 60 – 70 mT. The coercivity distribution changes notably for the heated sample SWH2Aa shown in (d). The bulk of the coercivity in the heated sample is 60 – 70 mT.

## S2.5 Quantum Diamond Microscopy

We used the quantum diamond microscope (QDM) at the Harvard Paleomagnetism Laboratory to acquire high-resolution magnetic field maps of olivine crystals IM1Be and IM3Ba from the Imilac pallasite (IM). Before imaging, the samples were given a 300 mT IRM out of the plane. Samples were polished and mounted in epoxy. The polished surface was in contact with the sensing diamond containing nitrogen vacancies distributed uniformly in a 13  $\mu\text{m}$  layer, resulting in effective spatial resolution of  $\sim 7 \mu\text{m}$ . All images were taken in projective magnetic microscopy (PMM) mode with an instantaneous bias field of 0.9 mT cancelled to an effective bias field of  $< 1 \mu\text{T}$  during the experiments (Fu et al., 2020; Glenn et al., 2017).

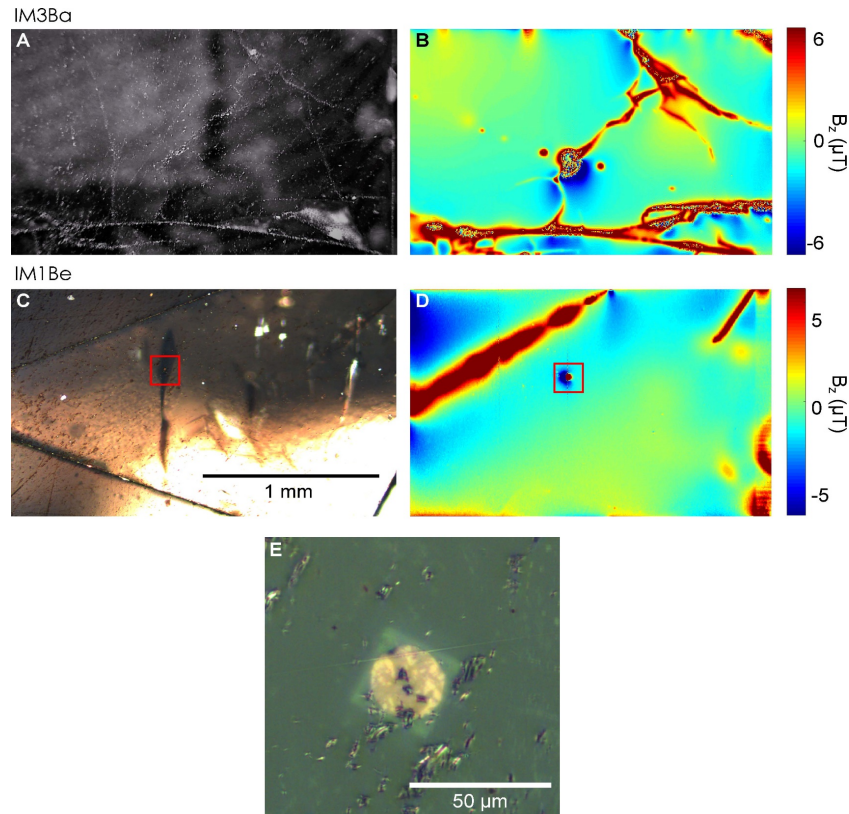


**Figure S14.** Reflected light and QDM images of the sources of magnetization in two olivines from the Imilac pallasite. **(a)** LED reflected light image of IM3Ba showing a network of cracks across the olivine. **(b)** QDM map of the same region of IM3Ba, showing the  $B_z$  component after applying a saturating field of 300 mT. The sources of magnetization are focussed along the cracks. **(c)** A reflected light microscope image of IM1Be. The red box highlights an inclusion of interest identified using the SEM (Figure S11). **(d)** QDM map of the same region of IM1Be, showing the  $B_z$  component after applying a saturating field of 300 mT. The magnetization is focussed along the edge of the sample, and on the inclusion of interest. **(e)** A reflect light image of the inclusion highlighted by the red box in c & d.

## S2.6 Vibrating Sample Magnetometry

Hysteresis properties of magnetic inclusions in olivines from the Imilac and Springwater pallasites were measured using a vibrating sample magnetometer (VSM). Measurements were conducted at room temperature using the Lakeshore PMC MicroMag system in the Department of Earth Sciences, University of Cambridge. The applied saturation field was 0.5 T. Hysteresis properties were investigated for a field of  $\pm 500$  mT in increments of 1.5 mT with an averaging time of 200 ms.

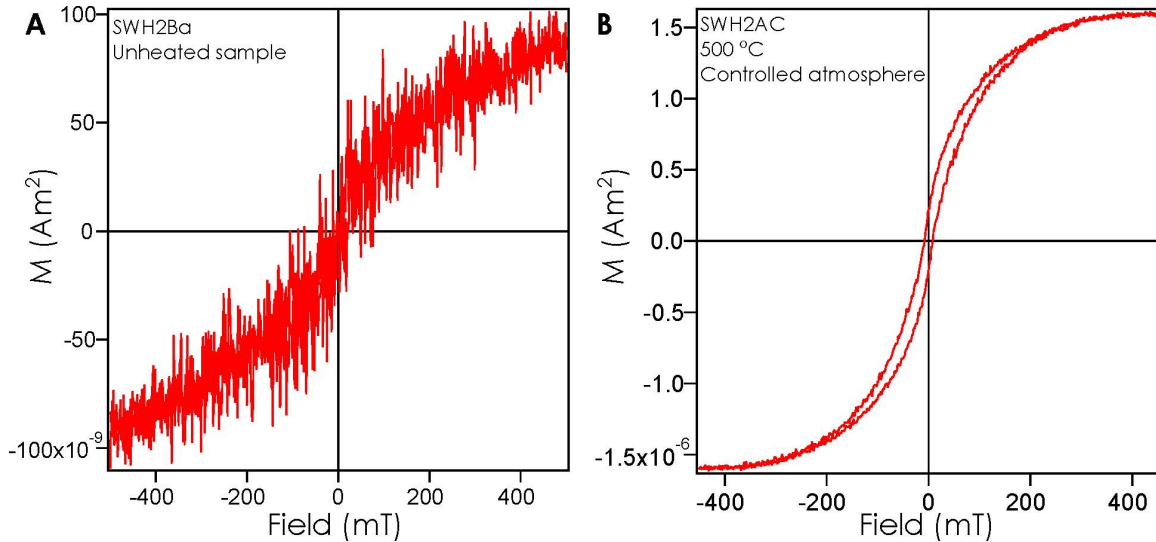


**Figure S15.** Hysteresis loops for two Springwater samples, corrected to remove the paramagnetic signal from the olivine crystal. **(a)** Sample SWH2Ba was not heated and contains no visible inclusions. It shows a weak magnetic moment and closed hysteretic behaviour. **(b)** SWH2Ac was heated up to 500 °C during the Thellier-Thellier experiment, in a controlled atmosphere. It shows open hysteretic behaviour indicative of the presence of single domain magnetic carriers.

## S2.7 IZZI Thellier-Thellier Experiments

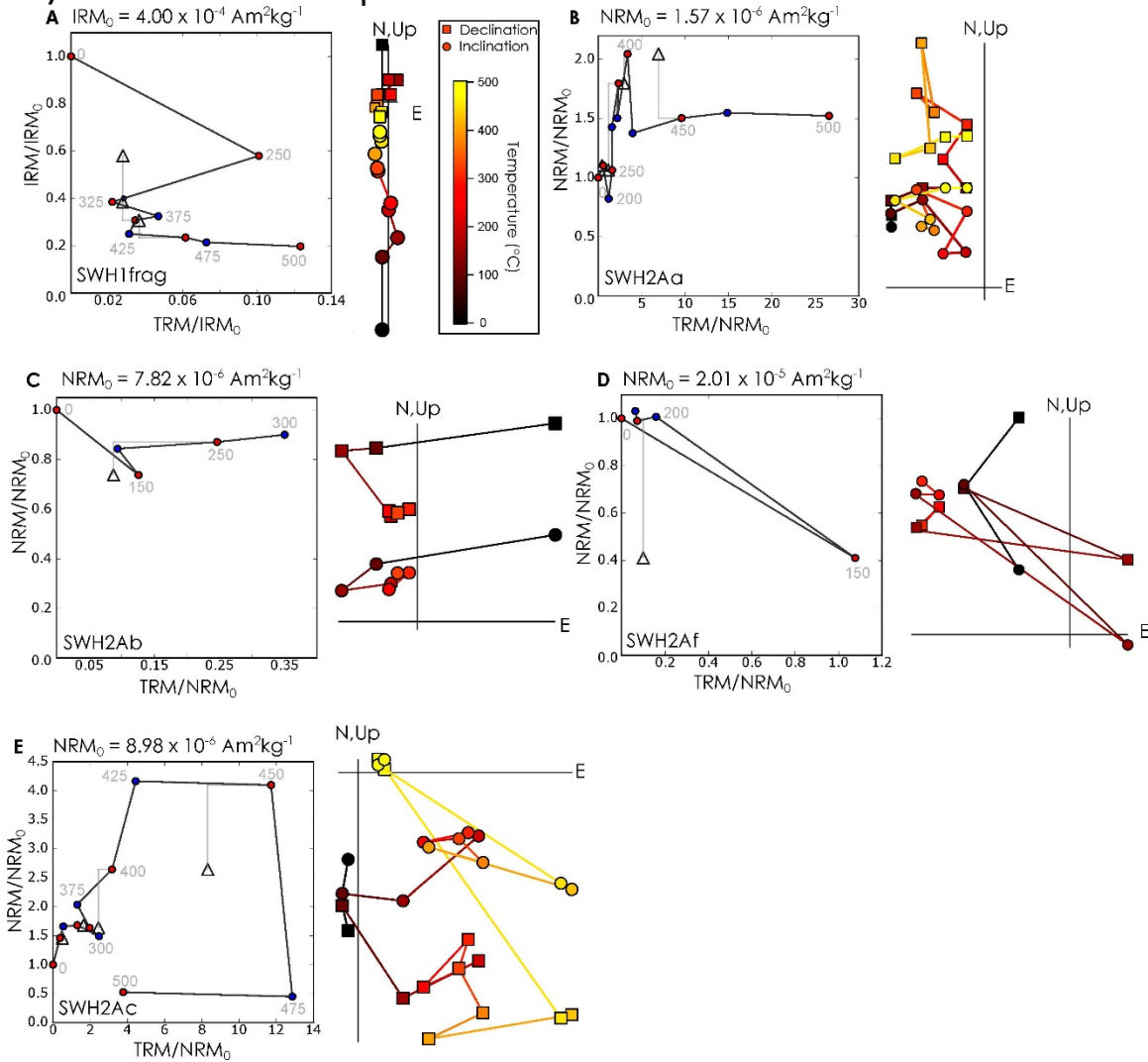


**Figure S16.** Springwater (SWH) Arai plots and Zijdeveld diagrams for IZZI Thellier-Thellier experiments conducted in a controlled atmosphere at the MIT Paleomagnetism Laboratory. The in-field was applied horizontally in the East direction. Sample SWH1frag was given a 400 mT IRM prior to demagnetisation.

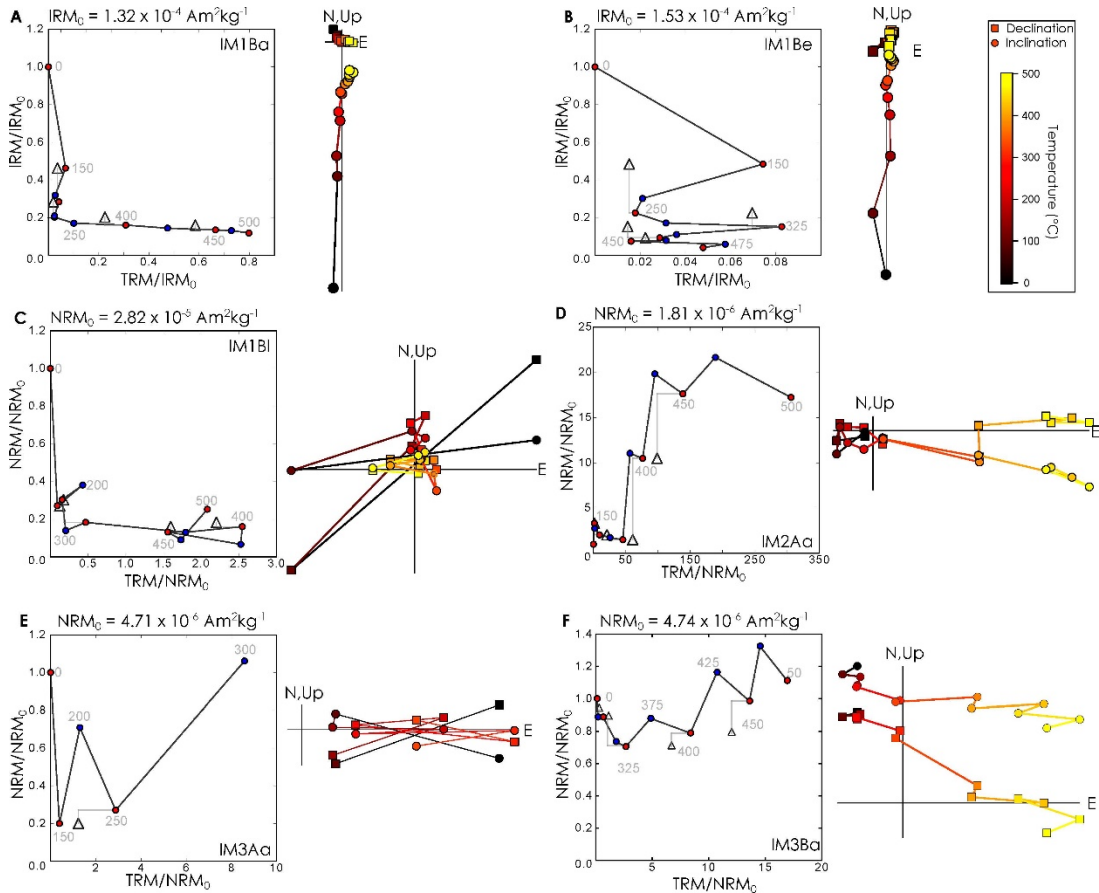


**Figure S17.** Imlac (IM) Arai plots and Zijdeveld diagrams for IZZI Thellier-Thellier experiments conducted in a controlled atmosphere at the MIT Paleomagnetism Laboratory. The in-field was applied horizontally in the East direction. Samples IM1Ba and IM1Be were given a 400 mT IRM prior to demagnetisation.

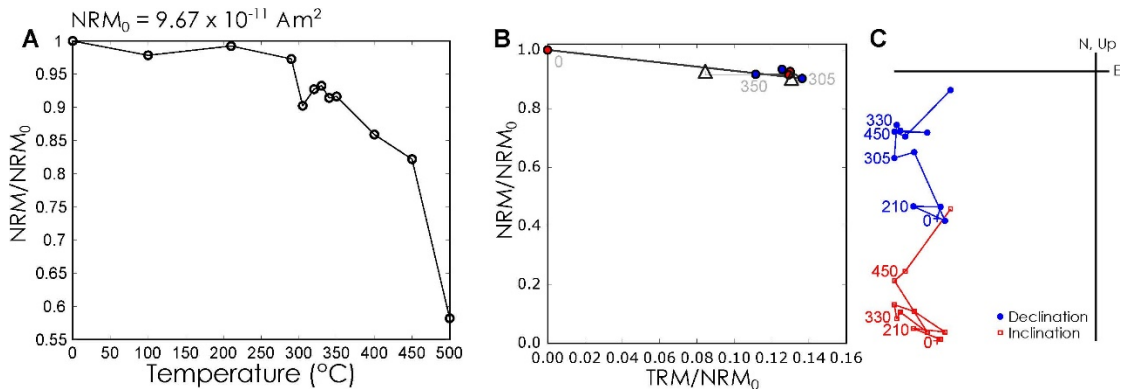


**Figure S18.** Thermal demagnetization data for specimen SWRTopD3, during IZZI Thellier-Thellier experiments conducted in air using laser heating. (a) Thermal demagnetization of the NRM up to 500 °C shown on a normalised moment vs temperature plot. The NRM value is  $9.67 \times 10^{-11} \text{ Am}^2$ . (b) Arai diagram for temperatures up to 350 °C. The pTRM check (at 320 °C) failed and the Thellier-Thellier experiment was not continued. (c) Zijdeveld diagram shows a potentially origin-trending component at temperatures > 400 °C.

Sample	pTRM check %			
	150 °C	250 °C	325 °C	400 °C
SWH1frag		-71.8	21.0	1.5
SWH2Aa	-30.3	-27.2	24.2	99.2
SWH2Ab	-63.3			
SWH2Af	-90.7			
SWH2Ac	4.1	25.4	-4.0	99.2
IM1Ba	-47.0	-54.4	822.7	89.7
IM1Be	-79.6	290.4	-82.5	-22.2
IM1BI	34.4	12.2	370.4	-37.3
IM2Aa	-1.1	121.7	33.5	29.4
IM3Aa	213.9			
IM3Ba	460.7	66.4	160.0	44.1

**Table S8.** pTRM check percentages were calculated for all samples of Springwater (SWH) and Imilac (IM) measured in Thellier-Thellier controlled-atmosphere experiments. pTRM checks were calculated as the TRM gained at the pTRM check as a percentage of the original TRM gained at that temperature step.

Sample	pTRM check %	
	305 °C	320 °C
SWRBotD2	196.0	
SWRTopD3	-3.7	-42.3

**Table S9.** pTRM check percentages were calculated for all samples of Springwater (SWR) measured in Thellier-Thellier CO<sub>2</sub> laser-heated experiments. pTRM checks were calculated as the TRM gained at the pTRM check as a percentage of the original TRM gained at that temperature step.

Text S3.

Thermal Model Results

Parent body radius (km)	Core radius (km)	Liquidus (K)	S content (wt%)	Onset of core nucleation (Myr)	End of core solidification (Myr)	Solidification time (Myr)	Max dynamo intensity ( $\mu$ -T)	Marijahlhti Time (Myr)	Brenham Time (Myr)	Springwater Time (Myr)	Ililac Time (Myr)	Esquel Time (Myr)	Dynamo Ft? (Y/N)	Model number
180	72	1400	27	128	213	85	15	89	102	128	164	212	N	0
185	88	1350	28	129	205	76	26	91	105	133	162	206	N	1
190	98	1340	29	127	202	75	34	93	108	139	166	203	N	2
190	86	1450	26	112	206	94	21	92	106	126	162	205	N	3
192	98	1350	28	128	207	79	33	92	108	130	166	206	N	4
200	110	1340	29	129	209	80	41	87	103	132	165	206	N	5
200	110	1350	28	126	207	81	41	87	103	132	165	206	N	6
200	100	1450	26	111	208	97	29	87	110	128	160	206	N	7
200	85	1480	25	120	233	113	16	87	110	130	166	212	N	47
202	105	1400	27	123	214	91	33	87	103	130	163	209	N	8
206	120	1350	28	122	204	82	50	90	107	129	163	205	N	9
208	115	1350	28	120	215	84	43	88	105	134	168	212	N	10
208	120	1350	28	126	210	84	48	89	107	128	164	205	N	11
210	125	1350	28	122	206	84	53	89	108	132	164	205	N	12
210	110	1480	25	118	233	115	24	89	105	122	160	207	N	43
213	128	1350	28	123	209	86	13	89	105	122	160	207	N	13
213	116	1400	26	116	216	96	54	92	105	133	166	204	N	14
218	140	1450	25	112	216	104	39	91	107	128	162	213	N	15
220	132	1450	26	115	221	105	39	91	107	128	162	213	N	16
220	100	1530	23	132	248	137	19	93	106	134	166	206	N	17
220	88	1550	22	114	267	153	12	92	103	126	158	206	N	41
225	135	1400	27	122	221	104	52	94	108	135	167	214	N	18
225	135	1400	27	122	221	104	52	94	108	135	167	214	N	19
230	138	1400	27	127	231	104	51	95	108	136	171	209	N	20
230	138	1450	26	110	218	108	51	95	108	136	171	209	N	21
230	120	1480	25	125	253	128	31	94	106	131	161	218	N	44
233	100	1550	22	119	283	164	15	95	103	131	161	218	N	33
235	141	1400	27	133	241	108	50	96	100	137	161	209	N	22
240	120	1550	22	106	259	153	26	96	100	133	166	209	N	23
240	130	1530	23	104	244	140	34	96	100	134	166	213	N	42
245	110	1570	20	108	290	182	17	88	101	126	157	209	N	34
250	150	1450	26	129	257	128	48	89	103	130	163	214	N	24
250	170	1400	27	114	218	104	46	92	110	138	171	207	N	52
258	155	1480	25	125	262	137	48	91	104	128	164	219	N	45
258	120	1570	20	115	311	196	19	90	104	126	162	205	N	35
260	130	1570	20	105	293	188	24	90	104	126	163	206	N	32
265	105	1590	18	111	363	252	10	92	105	127	161	208	N	25
265	150	1550	22	105	269	164	38	92	105	128	163	213	N	26
265	189	1450	22	131	277	177	45	94	106	129	166	219	N	46
265	180	1450	22	131	277	177	45	94	106	129	166	219	N	45
265	190	1330	28	133	326	203	50	100	110	140	170	233	N	53
270	130	1570	20	120	339	209	21	100	108	130	162	211	N	36
275	120	1590	18	107	361	264	14	93	107	130	165	209	N	27
275	205	1295	30	120	320	101	61	102	116	142	182	216	N	55
283	145	1570	20	139	337	217	25	102	109	123	158	206	N	37
290	174	1550	22	111	294	183	44	95	101	125	162	213	Y	28
295	150	1580	19	118	362	244	24	96	102	126	162	206	N	38
295	140	1590	18	111	383	272	19	96	102	126	162	206	N	29
307	160	1590	18	104	373	269	25	88	103	129	161	211	N	39
310	245	1275	30	149	401	112	72	109	121	157	190	240	Y	56
325	175	1590	18	110	401	291	28	90	106	132	156	205	Y	30
345	190	1590	18	119	438	319	29	93	109	126	161	212	Y	40
360	215	1590	18	109	421	312	39	94	106	124	160	204	Y	31
170	100	1200	31	112	419	307	14	93	108	128	154	203	0/8	48
210	150	1200	31	114	648	534	38	97	107	129	145	168	0/8	46
255	200	1200	31	125	956	831	80	109	121	136	159	167	0/8	50
303	250	1200	31	140	1319	1179	80	109	139	146	154	166	0/8	51

**Table S10.** Results for thermal models of the pallasite parent body. The upper part of the table corresponds to solutions for inner core nucleation. These are also valid for outer core nucleation, but the solidification timescales will be significantly longer. The lower part of the table corresponds to solutions for outer core nucleation only.

- Fu, R.R., Lima, E.A., Volk, M.W.R., Trubko, R., 2020. High-Sensitivity Moment Magnetometry With the Quantum Diamond Microscope. *Geochemistry, Geophys. Geosystems* 21, 1–17. <https://doi.org/10.1029/2020GC009147>
- Glenn, D.R., Fu, R.R., Kehayias, P., Le Sage, D., Lima, E.A., Weiss, B.P., Walsworth, R.L., 2017. Micrometer-scale magnetic imaging of geological samples using quantum diamond microscopy. *Geochem. Geophys. Geosyst.* <https://doi.org/10.1002/2017gc006946>
- Muxworthy, A.R., Williams, W., 2015. Critical single-domain grain sizes in elongated iron particles: implications for meteoritic and lunar magnetism. *Geophys. J. Int.* 202, 578–583. <https://doi.org/10.1093/gji/ggv180>
- Tikoo, S.M., Weiss, B.P., Buz, J., Lima, E.A., Shea, E.K., Melo, G., Grove, T.L., 2012. Magnetic fidelity of lunar samples and implications for an ancient core dynamo. *Earth Planet. Sci. Lett.* 337–338, 93–103. <https://doi.org/10.1016/j.epsl.2012.05.024>